



POLITECNICO
MILANO 1863

SCUOLA DI INGEGNERIA INDUSTRIALE
E DELL'INFORMAZIONE

Synchrotron-Based Study of Lithium-Ion Battery Failure: Pipeline for Agglomerate Segmentation and Analysis

TESI DI LAUREA MAGISTRALE IN
ENGINEERING PHYSICS - INGEGNERIA FISICA

Author: **Matteo Venturelli**

Student ID: 995709

Advisor: Prof. Giacomo Claudio Ghiringhelli

Co-advisors: Matilda Fransson, Ludovic Broche

Academic Year: 2022-2023

Abstract

Prevention and mitigation of thermal runaway presents one of the greatest challenges for the safe operation of lithium-ion batteries. At ESRF, high-speed synchrotron X-ray computed tomography and radiography are used to track the evolution of lithium-ion battery internal structure during thermal runaway. Agglomerate formation inside the cells is investigated for the first time, as it might yield new insights on thermal runaway. This work presents a pipeline for the segmentation and analysis of agglomerates in high-speed tomography data. The pipeline is based on a combination of image processing techniques, including thresholding, morphological operations, and connected component analysis. Segmentation results are presented and discussed, comparing different failure initiation methods and battery models. The results of this work are expected to provide a valuable framework for future research in this field.

Keywords: lithium-ion battery, thermal runaway, tomography, segmentation

Abstract in lingua italiana

La prevenzione e mitigazione del runaway rappresenta una delle maggiori sfide per il funzionamento sicuro delle batterie agli ioni di litio. All'ESRF, la tomografia computazionale e la radiografia ad alta velocità sono utilizzate per tracciare l'evoluzione della struttura interna delle batterie agli ioni di litio durante il runaway. Per ottenere una migliore comprensione di questo fenomeno, per la prima volta viene condotto uno studio sulla formazione di agglomerati all'interno delle batterie. Questo lavoro presenta una pipeline per la segmentazione e l'analisi di agglomerati presenti in dati di tomografia ad alta velocità, basata su una combinazione di tecniche di elaborazione delle immagini quali thresholding, operazioni morfologiche e analisi dei componenti connessi. I risultati della segmentazione sono presentati e discussi, confrontando diversi metodi di avvio del guasto e modelli differenti di batteria. I risultati di questo lavoro potrebbero fornire una base preziosa per ricerche future in questo campo.

Parole chiave: batterie agli ioni di litio, runaway, tomografia, segmentazione

Contents

Abstract	i
Abstract in lingua italiana	iii
Contents	v
Introduction	1
1 Lithium-ion Batteries	3
1.1 Overview	4
1.2 Positive Electrode	5
1.3 Negative Electrode	6
1.4 Electrolyte	7
1.4.1 Solvents	8
1.4.2 Conducting Salts	10
1.4.3 Additives	11
1.5 Separator	12
1.6 Current Collectors	13
1.7 Cell Geometries and Designs	14
2 Battery Failure	17
2.1 Thermal Runaway	18
2.1.1 Causes for Thermal Runaway	18
2.1.2 Semenov Model	20
2.2 Safety Standards	21
2.2.1 Safety Tests	22
2.2.2 Hazard level	26
2.3 Safety Features in Commercial Batteries	26
3 Synchrotron X-Ray Imaging	29

3.1	European Synchrotron Radiation Facility (ESRF)	30
3.1.1	Beamline ID19	31
3.2	X-ray Computed Tomography	32
3.2.1	Attenuation Contrast CT	34
3.2.2	Phase Contrast CT	35
3.2.3	Reconstruction Algorithms	37
3.3	High-speed Lithium-ion Battery Tomography	42
4	Developed Software	45
4.1	Segmentation	46
4.1.1	Threshold computation	49
4.1.2	3D Segmentation	49
4.1.3	Label propagation	51
4.1.4	Filtering	52
4.2	Feature extraction	53
4.3	Visualization	55
4.3.1	2D Visualization with Napari Viewer	55
4.3.2	3D Visualization with Blender	56
5	Results and Discussion	59
5.1	Initiation method comparison	59
5.2	P28A - VCT5A comparison	62
6	Conclusions and Future Developments	65
 Bibliography		 67
A	LIB energy balance	77
B	LIB chemical reactions	81
List of Figures		85
List of Tables		87
Acknowledgements		89

Introduction

The alarming acceleration of climate change, underscored by escalating CO₂ emissions, presents a formidable challenge to global environmental stability. The transportation sector, a significant contributor to these emissions, stands at the crossroads of urgent reform, necessitating a pivot towards sustainable solutions. The growing demand for electric vehicles as an alternative to internal combustion engine vehicles underscores the need for sustainable energy solutions.

Lithium-ion batteries, the primary energy storage technology for electric vehicles, have emerged as a key enabler of this transition. Their high energy density, rechargeability, and relatively low environmental impact compared to traditional fossil fuels make them an attractive solution for reducing CO₂ emissions in the transportation sector. Despite their efficiency as an energy storage system, lithium-ion batteries exhibit instability outside of normal operating conditions, particularly due to thermal runaway, a catastrophic failure mode not fully understood in existing literature.

Addressing this shortfall, high-speed X-ray imaging at the European Synchrotron Radiation Facility (ESRF), in collaboration with the Fraunhofer Institute for High-Speed Dynamics (EMI) and University College London (UCL), aims to grasp new insights on thermal runaway dynamics. Within this context, my work at the ID19 beamline focuses on post-processing and analyzing high-speed tomography data to segment and characterize the agglomerates that form inside batteries during failure events, contributing essential findings to enhance lithium-ion battery safety.

The thesis is structured to provide a comprehensive understanding of lithium-ion batteries and their critical role in addressing climate change through sustainable transportation solutions. It begins with an overview of these batteries, detailing their working principles and components. Subsequent chapters delve into battery failure mechanisms, safety regulations, and testing protocols to ensure reliability and safety. A significant focus is placed on the application of synchrotron imaging at ESRF and phase contrast computed tomography alongside the experimental setup. The development of the segmentation algorithm is then explored, followed by a discussion on the extraction and visualization of

agglomerate features. Finally, segmentation results are presented and discussed, offering new insights into thermal runaway.

This research is significant in its potential to contribute to the understanding of lithium-ion batteries failure mechanisms, thereby enhancing their safety and reliability. The development of a robust segmentation algorithm and the detailed analysis of agglomerate features are expected to provide a valuable framework for future research in this field.

1 | Lithium-ion Batteries

The Earth stands at a critical juncture in its history, where the consequences of human activity on the environment have reached a crossroads of global significance. Climate change, driven primarily by the relentless emission of greenhouse gases, has manifested itself in increasingly severe weather patterns, rising sea levels, and ecological disruptions. The urgency of the situation cannot be overstated, as nations grapple with the complex challenge of reducing carbon dioxide (CO_2) emissions to mitigate the impending climate crisis [1, 2, 3].

The dire need for sustainable energy solutions has never been more evident. Various sectors of the economy are challenged to reduce their carbon footprint in order to restrict their impact on climate change. The transport sector was responsible for 23% of global emissions from fuel combustion in 2021 and emerges as a critical contributor to the climate change predicament [4].

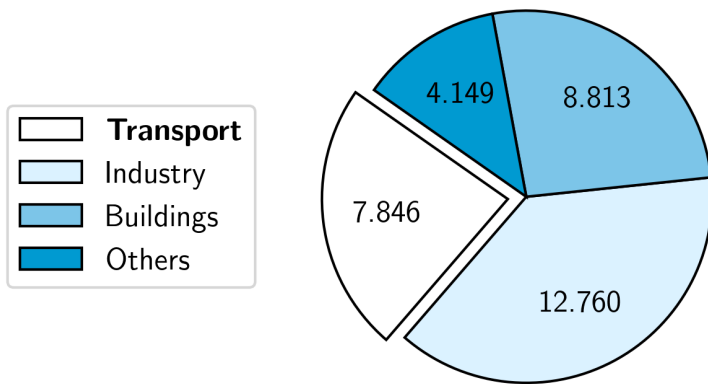


Figure 1.1: 2021 Global CO_2 emissions from fuel combustion by sector [Gt CO_2]. Adapted from: IEA (2023) [4].

As societies evolve and the global population continues to grow, the demand for transportation, particularly in the form of automobiles and other fossil-fuel-reliant means, has risen dramatically. Innovative solutions are crucial to decouple the connection between

personal mobility and CO₂ emissions. Electric vehicles (EVs) have emerged as a promising alternative to traditional internal combustion engine vehicles. They offer the potential to revolutionize the way we commute, significantly diminishing the transportation sector's contribution to carbon emissions.

At the heart of the electric vehicle industry's transformation lie lithium-ion batteries (LIBs). These energy storage devices have rapidly gained prominence as the primary means of powering EVs [5, 6]. The suitability of LIBs for this role is driven by their high energy density, rechargeability, and relatively low environmental impact compared to conventional fossil fuels [7]. As we explore the potential of lithium-ion batteries, it becomes evident that their development and adoption may hold the key to mitigating the environmental impact of the transportation sector.

The shortcomings of LIBs are their narrow operational temperature range and charge-discharge rates. The capacity of the battery degrades faster if working at a high temperature, and the lifetime is shortened, too [8, 9]. When LIBs are subjected to conditions outside of their optimal operating window, they may fail through a rapid self-heating or thermal runaway, which may ignite the surrounding materials [10]. Hence, LIBs require meticulous safety testing in order to guarantee safe use in all usage frameworks. Safety tests must produce reliable parameters to enable satisfactory evaluation and classification of safe battery specifications. The consumer and industrial market demands safe, low-cost, high-power batteries produced with low environmental impact, using sustainable components that enable easy recycling [11].

In the following sections the functioning of lithium-ion batteries is described, followed by a discussion of the safety and degradation issues that arise in LIBs.

1.1. Overview

A lithium-ion battery consists of two electrodes, an electrolyte, a separator, two current collectors and a metal casing (Figure 1.2). The positive and negative electrode materials are powders that are applied as coatings on current collector foils, resulting in composite electrodes. The ion-conducting electrolyte (which contains a dissociated lithium conducting salt) and the separator (an electrolyte-permeable membrane to electrically isolate the two electrodes) are situated between the two electrodes [12].

The electrolyte facilitates the movement of lithium ions while compelling electrons to travel through an external circuit to perform work. Metallic current collectors deliver electronic current from/to the redox centers of the electrodes to/from the external circuit.

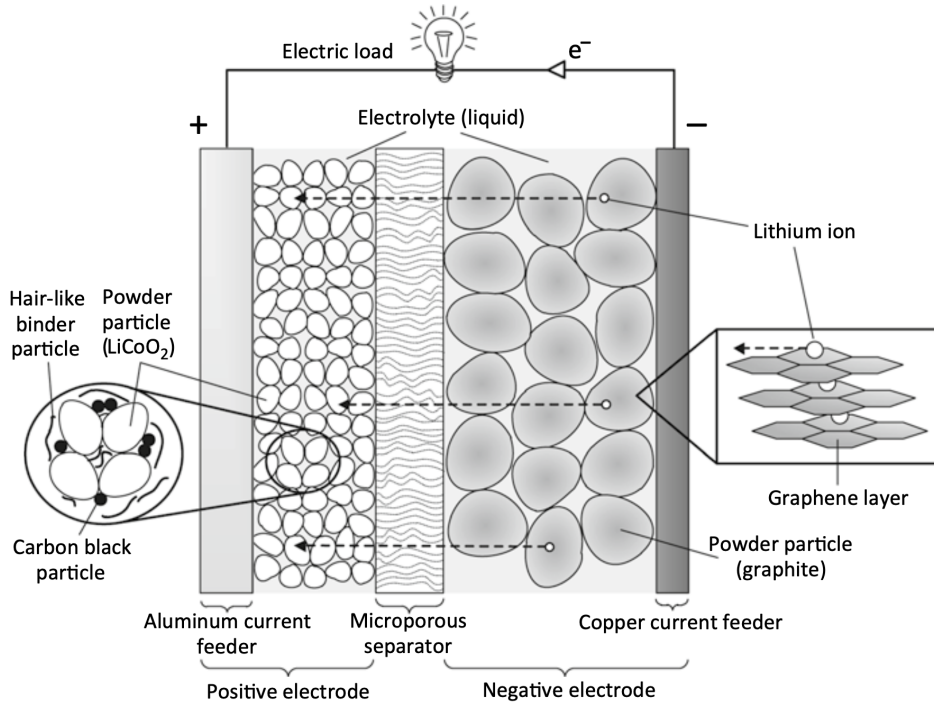


Figure 1.2: Components of a traditional lithium-ion battery during discharging. Source: Korthauer (2018) [7].

These elements are used to produce cylindrical, prismatic and pouch cells. Depending on the application, a single battery cell could be used or several cells could be connected either in series or parallel, forming a module. Several connected modules form a battery system for auto-motive applications [7, 12].

1.2. Positive Electrode

Lithium transition metal compounds are employed as positive electrode materials. These composites can develop mixed crystals over an ample composition range and can deintercalate lithium ions from the structure during the charging process. The traditional positive electrode material is lithiated cobalt oxide, LiCoO_2 . It has a layered structure with alternating cobalt, oxygen, and lithium ion layers. During charging, lithium leaves the crystal (deintercalation); during discharging, it returns (intercalation). However, only 50% of the lithium may be utilized. If more than half of the lithium leaves the crystal, the structure may collapse and liberate oxygen. This can cause thermal runaway, as oxygen is able to burn the electrolyte [7, 13].

For complete discharging, the reaction at the positive electrode is:



Thus for one mole (7 g) of active lithium, two moles (189 g) of $\text{Li}_{0.5}\text{CoO}_2$ are needed as host for lithium during discharge.

The use of cobalt oxide as positive electrode material can raise safety concerns. If it is kept “fully” charged as $\text{Li}_{0.5}\text{CoO}_2$, it reacts slowly with the electrolyte, thus losing performance. If it is slightly overcharged, there is a clear loss in capacity and service life. In case of severe overcharging, the cobalt oxide crystal collapses which can cause thermal runaway and fire. Overcharging easily happens, as there is no obvious voltage difference between normal charging and overcharging. Cobalt oxide’s high cost is attributed to the scarcity of cobalt ore, a situation aggravated by increasing demand where economies of scale offer no relief. Additionally, the toxicity of cobalt poses significant concerns.

The main commercial alternatives for cobalt oxide are listed in Table 1.1. Each of the alternative materials solves some of the problems but they all are compromises. LMO is safer and very cheap but has a limited service life. NCM is safer and cheaper, but has a sloping discharge voltage. NCA is cheaper and lighter (more specific capacity, mAh/g) but it is hardly safer. LFP is very safe and slightly cheaper, but it gives 0.5 V lower voltage than cobalt oxide. At the moment, NCM and LFP seem to be the most promising candidates for large-scale batteries [13, 14].

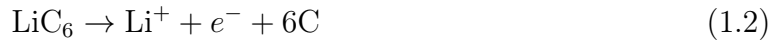
Compound	Abbreviation	Chemical structure
Manganese oxide	LMO	LiMn_2O_4
Nickel manganese cobalt oxide	NCM	$\text{LiNi}_{1/3}\text{Mn}_{1/3}\text{Co}_{1/3}\text{O}_2$
Nickel cobalt aluminum oxide	NCA	$\text{LiNi}_{0.8}\text{Co}_{0.15}\text{Al}_{0.15}\text{O}_2$
Iron phosphate	LFP	LiFePO_4

Table 1.1: Commercial alternatives for cobalt oxide. Source: Korthauer (2018) [7].

1.3. Negative Electrode

By far the most common negative electrode material is graphitic carbon. It has carbon atoms in parallel graphene layers. During charging, the lithium ions intercalate between the graphite layers. During discharging, lithium leaves the graphite. Unlike cobalt oxide,

graphite is stable even without lithium, so it can be almost completely discharged. For complete discharging, the reaction at the negative electrode is:



Thus for one mole (7 g) of active lithium, there are six moles (72 g) of carbon that act as host for the lithium during charging [7].

Graphite as negative electrode is not safe either. For graphite, the lithium intercalation potential is only about 80 mV more positive than the lithium metal plating potential. Even a small design failure or charging error causes deposition of metallic lithium on the electrode surface. Small amounts of metallic lithium increase the reactivity of the graphite surface, thus consuming electrolyte in secondary reactions. Large amounts of deposited lithium metal can grow as metallic peaks, “dendrites”, that short-circuit the negative and positive electrodes. This might cause excess heating and ignite the electrolyte resulting in a fire.

The potential of lithiated graphite is far beyond the stability window of the common electrolytes. During the first charging of the battery, graphite reacts with the electrolyte, building a protective layer on the graphite surface. This solid electrolyte interface (SEI) layer should prevent further secondary reactions. However, some secondary reactions take place throughout the lifetime of the battery, reducing its cyclic and calendar life.

Some commercial alternatives for graphite exist. Soft and hard carbons are used due to their slightly more positive intercalation potentials. This means less risk of lithium metal deposition and a possibility of faster charging. However, the energy density is considerably lower when these materials are used. Lithium titanate is a very safe negative electrode material with an amazingly long service life, but the 1.4 V lower cell voltage limits the use of lithium titanate to very few applications. The newest commercial alternative, silicon, gives a formidable energy density, but low stability limits its service life [14, 15].

Graphite is cheap and lightweight, especially when compared to cobalt oxide. Therefore, it can be expected that graphite retains its position as standard negative electrode material in the near future [7].

1.4. Electrolyte

Electrolytes are an essential component of a lithium-ion battery. The requirement profile of the perfect electrolyte is manifold and encompasses, among other things:

- high conductivity across a wide temperature range (-40°C to 80°C);
- cycling stability over several thousands of cycles;
- chemical/electrochemical compatibility with the electrode and inactive materials;
- risk minimization of thermal runaway and other hazardous reactions during battery operation;
- ecological sustainability;
- balance between cost and performance.

The tool box for each electrolyte for lithium-ion batteries consists of three classes of materials: conducting salt, organic aprotic solvents, and additives. It is the combination of these components which largely determines the physico-chemical and electrochemical characteristics of the electrolyte and contributes to fulfilling the above-mentioned objectives.

At the same time, the electrolyte is not an independent component of the cell. It needs to be chosen in dependence on the materials for the anode and the cathode side. That, in turn, calls for close collaboration between the electrolyte manufacturer and the cell and battery developers [7].

1.4.1. Solvents

In lithium-ion batteries highly reductive materials are used for the negative electrode and highly oxidizing components for the positive electrode. This is the reason why solvents with an active acidic proton are unsuitable. This would immediately lead to a development of hydrogen. The same reason excludes water as a solvent. Other mandatory requirements for the solvent are:

- high permittivity ϵ : the solvent must be able to dissolve lithium salts in a sufficiently high concentration;
- low viscosity η : unimpeded ion transport in the electrolyte is needed, especially at low temperatures and for high-voltage applications;
- inertia towards all other cell components in all operating conditions;
- low melting point T_m and high boiling point T_b : the electrolyte must be liquid over the entire operating temperature range of the battery;
- low toxicity and low cost.

Two classes of organic solvents that are simultaneously aprotic and highly polar have gained recognition as suitable materials for lithium-ion batteries: ethers and esters, including organic carbonates.

Ether-containing electrolytes for the most part exhibit a low viscosity and therefore a very high conductivity, but their electrochemical stability is restricted and they are already oxidized at potentials around 4 V vs. Li/Li⁺. With the introduction of 4-V transition metal oxides as positive electrode materials, ethers have therefore disappeared as solvents for high-energy lithium-ion batteries.

Esters, especially organic diesters of carboxylic acid (so-called carbonates), are current state of the art. In general, the following are employed: blends of cyclic carbonates (e.g., ethylene carbonate [EC] and, to some extent, propylene carbonate [PC]) that exhibit a high dipole moment at moderate viscosity. Also, open-chain carbonates (dimethyl carbonate [DMC], diethyl carbonate [DEC], and ethyl methyl carbonate [EMC]) are used, which exhibit a moderate dipole moment at low viscosity [16, 17, 18].

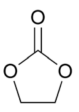
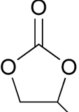
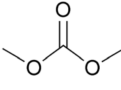
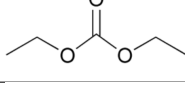
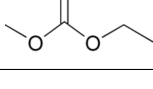
Solvency	Structure	Melting point [°C]	Boiling point [°C]	Viscosity (25 °C) [cP]	Permittivity (25 °C)
EC		36	247-249	1.9 (40 °C)	90 (40 °C)
PC		-48	242	2.53	65
DMC		2-4	90	0.59	3.1
DEC		-43	125-129	0.75	2.8
EMC		-55	108	0.65	3.0

Table 1.2: Psycho-chemical characteristics of selected battery solvents. Source: Korthauer (2018) [7].

1.4.2. Conducting Salts

The electrolyte provides for the lithium ion transport between the electrodes. Therefore, a suitable lithium salt must provide maximum solubility and complete dissociation in aprotic solvents to ensure a high lithium-ion mobility. Very high electrochemical anion stability is also needed, in addition to high chemical stability in respect to the solvent. This requirement profile leads to mostly complex anions in which the negative charge is distributed to a high extent across the anions. This reduced charge density in turn causes a low attraction between the anion and the lithium cation, which determines the free movement of the cation and is therefore necessary for a high mobility.

In terms of the compounds possible in principle, lithium hexafluorophosphate (LiPF_6) plays a special role. Nowadays, commercial lithium-ion batteries predominantly use LiPF_6 . This is due to an unparalleled combination of characteristics rather than a single outstanding feature, and also relies on the willingness to overlook certain drawbacks.

Having a conductivity of 8 to 12 mS/cm (room temperature, 1 mol/l), LiPF_6 forms highly conductive electrolytes in blends of organic carbonates. These electrolytes are, in addition, electrochemically stable up to almost 5 V vs. Li/Li^+ . LiPF_6 is one of the few conducting salts that very effectively prevent the corrosion of the aluminum current collector of the positive electrode at potentials above 3 V vs. Li/Li^+ . Since today's lithium-ion technology has been developed based on this conductive salt, the production process has been improved over decades, and high-purity LiPF_6 has been available on an industrial scale for more than 30 years.

The limited chemical and thermal stability of LiPF_6 are its main disadvantages. In its pure form it very slowly disintegrates into traces of lithium fluoride (LiF) and phosphorous pentafluoride (PF_5), creating an equilibrium. High temperatures promote this process.



Lithium-bis(trifluoro- methylsulfonyl)imide (LiTFSI) and lithium-bis(fluorosulfonyl)imide (LiFSI) have increasingly been introduced into the market as alternatives to LiPF_6 . They are characterized by a high thermal stability, however they are not as electrochemically stable as LiPF_6 and are not as effective in preventing corrosion of the aluminum current collector. In addition, they are more expensive and less soluble in organic solvents. LiTFSI and LiFSI are therefore used in combination with LiPF_6 [16].

1.4.3. Additives

Additives mainly are employed to optimize the so-called solid electrolyte interface (SEI), the boundary surface between the negative electrode and the electrolyte. The SEI significantly influences service life and performance of the lithium-ion cell. Lithium ions do not exist in the form of “naked” cations in organic polar solvents, but rather as complex cation solvent adducts. This so-called solvate complex is many times larger than the naked lithium ion. Solvated lithium ions penetrate into the outer structures of the graphite anode during charging of the lithium-ion cell. The solvents (and in part also the anion of the lithium salt) degrade owing to the extremely reductive conditions and form hardly soluble precipitates. They accumulate on the electrode and in the outer structures of the graphite and form the layer that is called SEI. This layer is permeable for lithium ions. At the same time it is electrically isolating and prevents the direct contact of electrode and solvent, a characteristic that prevents further degradation of the solvent. All carbonates employed in lithium-ion batteries nowadays form an SEI. The quality and composition of the layer, however, strongly depend on the chosen solvent combination [7].

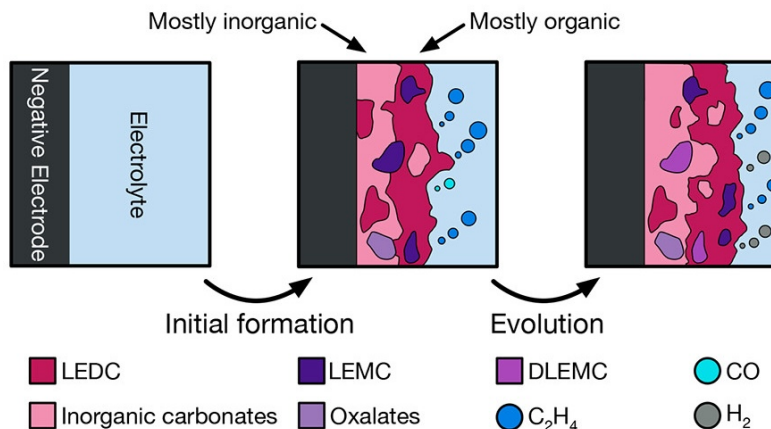


Figure 1.3: Mechanistic model of the SEI. Source: Spotte-Smith (2022) [19].

The SEI's structure and characteristics might be influenced significantly by the additives. The SEI additives must be more reactive electrochemically than all other components of the electrolyte in order for the SEI to be reduced during the first charging cycle of the lithium-ion cell before the solvents react. This way, an SEI is formed before the solvents react. The best-known example of this class of additives is vinylene carbonate. It is used in almost every commercial lithium-ion cell and leads to a significant improvement of the cycling stability. It becomes effective during the first charging and discharging cycles of the lithium-ion cell [16].

1.5. Separator

Battery separators are flat materials situated between the positive and negative electrodes of a battery cell. Their function is to prevent physical contact and, therefore, short circuits. At the same time, they must enable ions to be transported as freely as possible within the electrolyte between the electrodes. This is essential for charge equalization and the electrochemical cell to work. To achieve this, separators are usually porous flat designs filled with an electrolyte [7].

Property	Description
Thickness	The separators of consumer application lithium-ion cells are relatively thin. They have a thickness of less than μm . However, thicker separators (up to $40 \mu\text{m}$) are used for the production of large-size lithium-ion cells. These have considerably higher mechanical stability and puncture resistance.
Porosity	Standard separators for lithium-ion cells have a porosity of around 40%. Controlling the porosity is of great importance in separator manufacturing and immensely influences the porosity of the end product. In addition, high porosity enables a larger electrolyte reservoir. Non-uniform porosity, on the other hand, leads to non-uniform current densities which result in the electrodes aging more rapidly.
Pore size	The pores must be small enough to prevent an electrical connection caused by loose electrode particles. Also, they need to prevent dendrite growth in the lithium-ion cell. Separators with a thickness of $< 25 \mu\text{m}$ are assumed to have an average pore size in the submicron range. The pore size distribution in battery separators must be as homogeneous as possible, as is the case for requirements related to porosity. This enables a uniform current density and thus uniform aging of the cell.
Chemical stability	The separators must be chemically and electrochemically stable in both the battery and its electrolyte. In particular, the development of high-voltage materials has given rise to new requirements for separators.

Table 1.3: Separators essential properties. Source: Korthauer (2018) [7].

In lithium-ion cells, battery separators are mostly based on polyolefins into which submicron-sized holes are introduced by means of a physical process. These battery separators can be divided into two classes based on their production process: microporous polyolefin membranes and wet membranes. Resulting from their chemical and physical compositions, these two separator classes exhibit in part extremely different characteristics.

Microporous polyolefin membranes exhibit a thickness up to 12 to $40 \mu\text{m}$, a maximum pore size of $< 0.5 \mu\text{m}$, and a high tensile strength. The low thickness positively influences the energy density of the battery. The pore distribution protects them against dendrite for-

mation quite well. The disadvantages of these membranes are their low porosity (around 40%), low melting point (around 160 °C for PE), and very high shrinkage (20% at 120 °C/10 min) at higher temperatures. This is increasingly true for larger cells because they dissipate heat poorly. If the separator loses its structure, there will be contact between the electrodes and thus a reaction of the electrode materials. This can cause the battery to explode [7].

Wet membranes have a thickness of up to 25 μm , uniform pore distribution with short distances ($< 1 \mu\text{m}$), and high tensile strength. The low thickness positively influences the energy density of the battery. The short pore distances effectively prevent dendrites from forming. As with the microporous polyolefin membranes, the tensile strength is beneficial for producing cylindrical cells. The disadvantages of these membranes are their low melting point (around 135 °C) and very high shrinkage (7 to 30% at 120 °C/10 min) [20, 21].

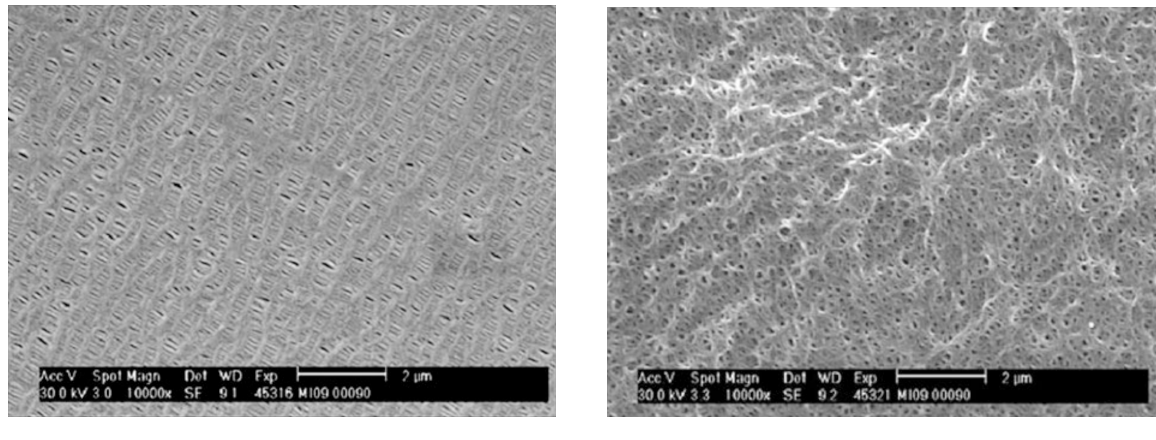


Figure 1.4: Scanning electron microscopic pictures of a microporous polyolefin membrane and a wet membrane. The samples were metallized with gold to achieve a higher resolution. Source: Korthauer (2018) [7].

1.6. Current Collectors

By enabling conduction of electrons between the electrodes and the battery terminals, the current collectors greatly impact the performance of the battery. The current collectors are viewed as un-active components of the cell but can however make up 15% of the cell weight. Properties such as electrochemical stability, electrical conductivity, mechanical strength, density, sustainability and cost has to be thoroughly evaluated. In conventional lithium-ion batteries the most commonly used materials are copper and aluminum foil

for the negative and the positive electrode respectively. A high electrical conductivity is required for efficient transportation of electrons through the external circuit of the battery.

As for any other component of the battery, the ability of the current collectors to sustain in an electrochemical environment and not to undergo undesired reactions is vital. Furthermore, it is crucial to maintain a satisfying adhesion between the current collectors and the electrodes; to achieve this, polymeric binders such as PVDF are commonly used. Both aluminum and copper show high electrical conductivity and valuable mechanical properties. The low density of aluminum ($2.70 \text{ g}\cdot\text{cm}^{-3}$) contributes to an increase in gravimetric energy density, while copper on the contrary has a high density of $8.96 \text{ g}\cdot\text{cm}^{-3}$. Consequently, for the case of the copper foil there is a trade-off between high electrical conductivity and thickness. In terms of heat generation, the current collectors act as efficient heat dissipators due to their high thermal conductivity and play an important role in the events leading up to a thermal runaway [22].

1.7. Cell Geometries and Designs

Battery cells come in various shapes and sizes, featuring diverse component assemblies and chemistries based on the manufacturer. The effectiveness of cell design is pivotal for ensuring safety and suitability in different applications. The selection of materials and dimensions significantly influences a battery's ability to prevent or minimize catastrophic events. To ensure optimal and secure functioning, meticulous consideration is given to the design of all aforementioned components and their collaborative functions to fit within the specified cell dimensions. Additionally, the choice of casting material and its thickness should be carefully designed to facilitate the handling of critical events by enhancing heat dissipation and pressure management.

All of today's lithium-ion cells exhibit metal-based housing and packaging material. One reason is that it prevents the entry of moisture into the cell, which would initiate a hydrolysis of the conducting salt LiPF_6 into hydrogen fluoride (HF). Another is the prevention of loss of solvent by means of diffusion from the cell. Only metal is able to fulfill these tasks. A housing made of pure plastics is not suitable because no plastic (not even polypropylene) is completely moisture leaktight. The solid metallic housings (hardcase) are typically made of aluminum or stainless steel [7].

The most common cell geometries are cylindrical, prismatic, and pouch cells. The main difference between the cell formats lies in the design of the cell casing and the arrangement of the cathode, anode, and separators.

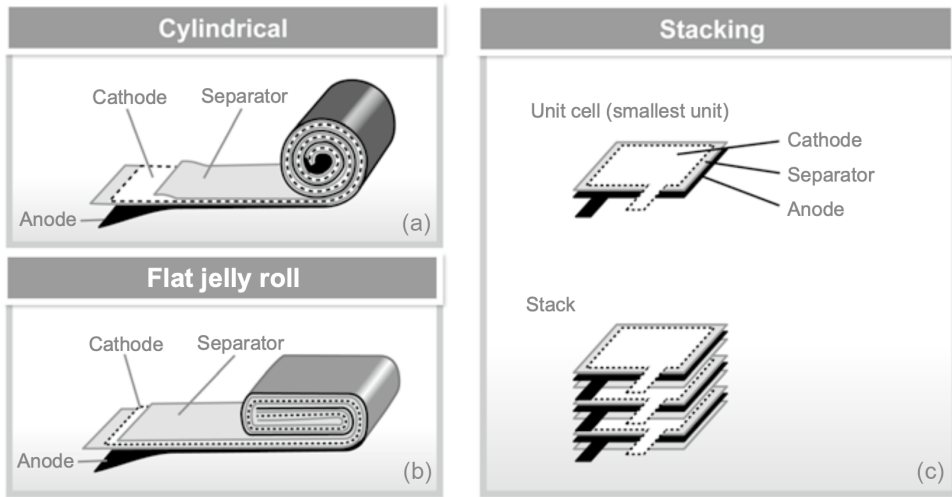


Figure 1.5: Inner structure of lithium-ion cells. Source: Korthauer (2018) [7].

The **cylindrical cells** (Figure 1.5a) are the oldest and most common cell type. The introduction on the market of a cylindrical round cell in a stainless steel housing for consumer applications by Sony ensued in 1991. The batteries measure 18 mm in diameter by 65 mm in length, giving them the name 18650 [7].

18650 battery is widely regarded as the most produced lithium-ion cell size. This cell type is used in many laptop computer batteries, cordless power tools, many electric cars, electric scooters, most e-bikes, older portable powerbanks, electronic cigarettes, portable fans and LED flashlights [23].

Cylindrical cells consist of a tubular cylindrical can and are crafted using a "jelly roll" technique. This involves creating a singular elongated "sandwich" by rolling together the positive electrode, separator, negative electrode, and separator into a single spool. An inherent advantage of cylindrical cells, in contrast to those featuring stacked electrodes, lies in their faster production speed. However, a notable drawback of cylindrical cells may manifest as a substantial radial temperature gradient within the cells under high discharge currents [24].

Cells possessing a cylindrical morphology incorporate safety mechanisms that will interrupt current flow and/or enable venting of gas to avoid overpressure of the can. Cylindrical cells have better thermal management efficiency because of small size, but low packaging efficiency because of their round cross-section [25].

Aluminium or steel cans are typically used for the housing of solid container-encased prismatic lithium-ion cells, more commonly called **prismatic cells** (Figure 1.5b). The metal can ensure structural stability, mechanical robustness, and humidity protection. In

addition, it allows for the use of safety features such as pressure relief vents, which are not possible in pouch cells. In some cases, prismatic cells may allow packaging to be more efficient than cylindrical cells because of their form factor [25].

The **pouch cells** (Figure 1.5c) employ a streamlined fold-stacking approach for individual sheets of both the positive and negative electrodes, enclosed in a lightweight foil casing. This configuration yields a cell characterized by high packing efficiency, flexibility, and low weight. The resulting compact and lightweight design contributes to an elevated volumetric energy density, cooling advantages, and adaptability for diverse applications due to its flexible nature. Nevertheless, the drawback of pouch cells lies in their limited physical strength, necessitating mechanical support in the form of a module or pack. Commonly addressed challenges include cell swelling during gas formation, which can alter the internal structure and pose risks to adjacent cells, thereby increasing the likelihood of failure and catastrophic events [26].

2 | Battery Failure

The increasing interest in lithium-ion batteries stems from their potential to offer efficient energy storage and contribute to environmental sustainability. Not only are LIBs widely employed in portable electronics like computers and cell phones, but they have also become integral to the power systems of electric and hybrid vehicles. The increasing popularity of LIBs in these applications can be attributed to their outstanding performance and high energy density [27]. Moreover, LIBs dominate the battery market for portable electronics, owing to inherent advantages such as high specific capacity and voltage, absence of memory effect, excellent cycling performance, minimal self-discharge, and a wide temperature range of operation [5].

No.	Date	Accidents Replay
1	Mar 2010	Two iPod Nano music players overheated and caught fire, Japan
2	Apr 2010	Acer recalled 2700 laptop batteries, as Dell, Apple, Toshiba, Lenovo and Sony did in 2006
3	Apr 2011	EV taxi caught fire, Hangzhou, China
4	Jan-Dec 2013	Three fire accidents of Boeing 747, happened in Boston America, Taka-matsu, Tokyo Japan, respectively
5	Oct-Nov 2013	6 Tesla Model S EV cars caught fire
6	Apr 2015	EV bus caught fire during charge, Shenzhen, China
7	May 2016	The storage room of the LIB caught explosion, Jiangsu, China
8	Aug 2016	Samsung Note 7 smart phone explosion
9	May 2017	Panasonic announced to recall over 270 thousand LIBs
10	Oct 2017	EV car caught fire, Austria
11	Jan 2018	Tesla Model S EV car self-ignited, China
12	Jul 2018	4 MW/12 MWh energy storage system (ESS) caught fire and explosion, Korea
13	Jul 2018	Electric scooter caught fire and explosion during charging, China

Table 2.1: Lithium-ion battery fire and explosion accidents in the past few years. Source: Wang (2019) [28].

Despite these merits, the broader expansion of the LIB market, especially in electric vehicles, faces significant challenges due to safety concerns [29, 30, 31]. Recent years have witnessed numerous recalls of LIBs, prompted by incidents of explosions and fires (Table 2.1), leading to substantial economic repercussions in related market sectors and tarnishing the reputation of LIBs [32, 33]. As a result, there is a growing emphasis on addressing LIB safety issues, with the development of numerous safety strategies aimed at mitigating the risks associated with these batteries.

2.1. Thermal Runaway

Rising battery temperature under extreme conditions could trigger undesirable parasitic reactions, causing thermal runaway, where battery heat generation cannot be controlled [34].

Generally, thermal runaway occurs when the heat generated by exothermic reactions is not offset by the heat losses to the environment. This accumulated heat drives the temperature increase which, in turn, produces an exponential increase in the reaction rates. If the rate of heat generation exceeds the rate of heat dissipation into the environment, the temperature will continue rising. When reaching some critical temperatures, especially the collapse temperature of separator, the cell will breakdown.

2.1.1. Causes for Thermal Runaway

In the normal voltage and temperature range, only Li^+ shuttle occurs in the electrolyte during the insertion/extraction cycles at the cathode and anode. At high-temperature and high-voltage conditions, the electrochemical reactions become more complex, including decomposition of the solid electrolyte interface (SEI) film, oxygen release at the cathode side, and additional electrolyte/electrode parasitic side reactions [35]. SEI film decomposition and interfacial reactions initially accelerate the temperature increase, thereby increasing risks of oxygen release from the active cathode materials. These reactions can eventually lead to LIB thermal runaway, which could cause battery rupture and explosion due to the reaction of hot flammable gases from the battery with the ambient oxygen [36].

During mechanical (damage to shell casing, compression, punching, and twisting of cells), electrical (overcharge/discharge and short circuit), and thermal abuse (thermal shock and local heating) situations, which could occur during accidents, thermal runaway will occur even quicker [37, 38, 39].

Figure 2.1 shows the origins of thermal runaway in LIBs, including side reactions of electrolyte, cathode, anode, and interfacial reactions at the surface of electrodes and Li plating. These side reactions are triggered by mechanical, thermal, and electrical abuse. Breakage of the separator and the oxygen evolution from the cathode side are the root causes to batteries' thermal runaway (as shown in the solid lines of Figure 2.1d).



Figure 2.1: Schematic of the causes of LIBs thermal runaway. Source: Chen (2020) [32].

The five types of causes for thermal runaway are listed below.

1. **Uncontrollable internal heat generation** causes oxygen release from the cathode material, leading to numerous side reactions [40];
2. **Separator defects** (due to thermally-induced shrinkage or mechanical damage) create short circuits in the battery and rapid discharge of the energy stored in it, accompanied by undesirable chemical chain reactions and release of massive amounts of heat [41];
3. **Electrical abuse**, especially in a high state of charge, causes electrolyte decomposition at the cathode interface. This leads to heat accumulation and consequently release of oxygen from the cathode and damage to the separator [42];
4. **Thermal abuse** gives rise to electrochemical side reactions and heat generation. If the heat cannot be dissipated quickly enough, the separator will shrink or rupture [43, 44];

5. **Mechanical abuse** causes short circuits and/or air to penetrate the battery, originating a failure [45].

2.1.2. Semenov Model

The Semenov plots [46] shown in Figure 2.2 can be used to further illustrate the dynamics of the thermal runaway. The curved line (line 4) represents the heat generation due to the exothermic reaction (exponential function, following the Arrhenius law), while the straight lines 1, 2 and 3 represent the heat loss under different ambient temperatures (ambient temperature A , B and C , respectively) which is a linear function following the Newton's law of cooling.

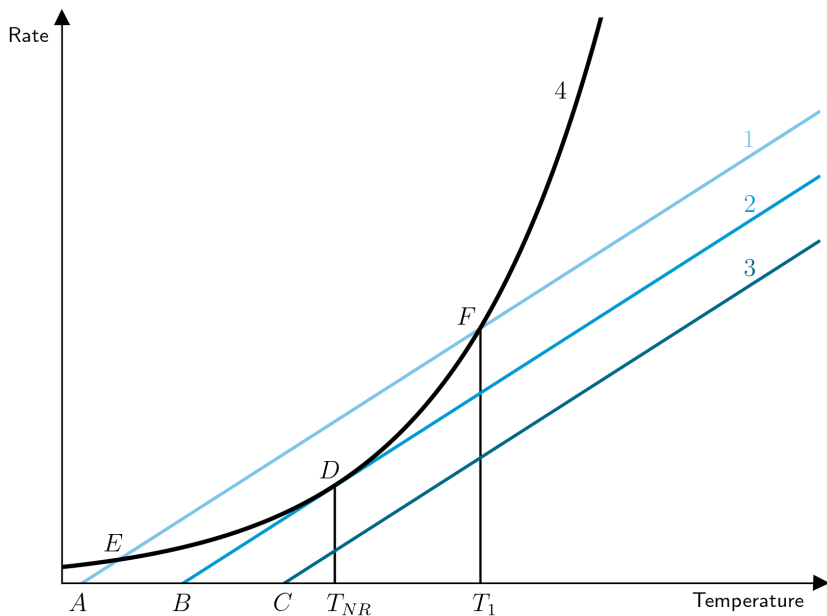


Figure 2.2: Temperature dependence of reaction rate and heat loss from a system at three ambient temperature: A , B and C . Adapted from: Semenov (2013) [46].

When the ambient temperature is A , there are two intersection points (E , F) between line 4 and 1, where the heat generation rate is equal to the heat loss rate. The lower point E is a stable thermal balance point. If temperature deviates upwards, the cooling rate is higher than the heat generation rate, so the system will return to point E . If temperature drops, the heat generation rate is higher than the cooling rate, so the system will return to point E again. Point F is an unstable and also an unreachable point, because the heat loss rate is higher than the heat generation rate before T_1 , so the system will cool to point E rather than heat to point F . When the ambient temperature increases to B , line 2 has one tangent point D with line 4. At this point, the heat loss rate is equal to

the heat generation rate, and once the system temperature increases a little, the system's temperature will continue to rise at a progressively higher rate. This critical equilibrium temperature is called the "Temperature of No Return, T_{NR} ", and the ambient temperature B is the self-accelerating decomposition temperature (SADT). LIB can be regarded as a reaction system, in which the heat comes from the electrochemical reactions between its components.

Semenov plots illustrate only a special case for LIB thermal runaway rather than a universal model. In the realistic reaction process, the system is hard to reach uniform temperature distribution, but Semenov model can simplify the problem. In fact, many realistic situations could be solved based on the assumption of uniform temperature distribution. Many investigators still assumed that the temperature inside the battery was spatially uniform before thermal runaway in external heating and self-heating test [47, 48].

Details regarding the energy balance and the chemical reactions taking place in lithium-ion batteries can be found in Appendix A and Appendix B, respectively.

2.2. Safety Standards

Safety standards and corresponding assessments have been established to analyze battery performance and key factors, aligning with the necessary safety requisites. The stringent and rigorous battery safety tests are designed to minimize the likelihood of safety issues in routine working conditions and ensure that batteries available on the market are of sufficient quality for intended purposes. Thanks to these measures, contemporary LIBs exhibit a significantly enhanced safety profile compared to their predecessors. Nonetheless, ongoing advancements are imperative to further improve battery safety standards [32].

Hence, various international organizations regulate battery safety, and governments of different countries have formulated standards in accordance with national requirements and conditions and have gradually improved the safety standards of lithium-ion batteries. Academics and industrial groups have also carried out extensive research on battery safety.

Most countries and international organizations have developed LIB safety oriented standards, which include:

1. Chinese standard GB/T 31485 [49];
2. Society of Automotive Engineers (SAE) standard 2464 [50];
3. International Electrotechnical Commission (IEC) standard IEC62133 [51];
4. United Nations (UN) standard UN38.3 [52];

5. Japanese Industrial Standard (JIS) C8714 [53];
6. Underwriters Laboratories (UL) standard UL2580 [54];
7. International Standardization Organization (ISO) standard ISO 16750-2 [55].

Since the various safety test standards apply different methodologies, a summary of some test requirements and comparisons of five test items are presented in Table 2.2.

	GB/T31485	IEC62133	UL2580	SAE J2464
Heating	Heating at 5 °C/min from 25 °C to 130 °C, hold for 30 mins	130 °C, 10 mins	150 ± 2 °C, 60 mins	Max. stable temperature
Short-circuit	Short circuit for 10 mins, $R \leq 5\text{m}\Omega$	80±20mΩ	Short with $R \leq 5\text{m}\Omega$ until explosion, fire or no temp change	$R \leq 5\text{m}\Omega$ for hard short; $R \geq 5\text{m}\Omega$ for soft short
Overcharge	100% SOC Overcharge to 1.5 V_{max} or charge for 1 hour at 1C	Overcharge to 250% SOC at 1C	Overcharge to 200% SOC at 1C	Overcharge to 200% SOC at 1C
Over-discharge	Over-discharge the 100% SOC cell at 1C for 1.5 hours	Over-discharge the 0% SOC cell at 1C for 90 mins	Over-discharge the 0% SOC cell at 1C for 90 mins	Over-discharge the cell to -100% SOC
Nail penetration	Penetration rate 25 mm/s, φ 5~8mm, 100% depth	/	80 mm/s, φ 3mm, 100% depth	80 mm/s, φ 3mm, 100% depth

Table 2.2: Testing standards comparison of selected items. φ represents the nail diameter.
Source: Chen (2021) [32].

2.2.1. Safety Tests

Analysis of the presence of various LIB defects and shortcomings can help to define specific LIB safety issues or hazards. Extensive testing uncovers these issues to assist efforts to ensure that future generations of batteries are safer and more reliable. In a safety test possible trigger modes are simplified so batteries thermal runaway characteristics are measurable in the laboratory. Laboratory environment test conditions must generally be more stringent than "real-world" conditions to ensure safety during actual use. For example, batteries being tested have to be maintained at a 100% state of charge (SOC). The three principles of operability, repeatability and reproducibility should be met in the process of formulating a safety standard.

Here follows a brief description of the main safety tests used to examine key LIB properties.

Electrical Abuse Tests

When a battery is in an overcharge or over-discharge state, or is undergoing a short circuit, it experiences electrical abuse, and a series of undesirable electrochemical reactions occurs in it.

There are many reasons for battery overcharging. One of the main reasons is the inconsistency of battery cells. If the voltage of any battery cell cannot be effectively monitored by the management system, there will be risks of its overcharging. Since excess energy is stored into the battery, overcharging is very dangerous.

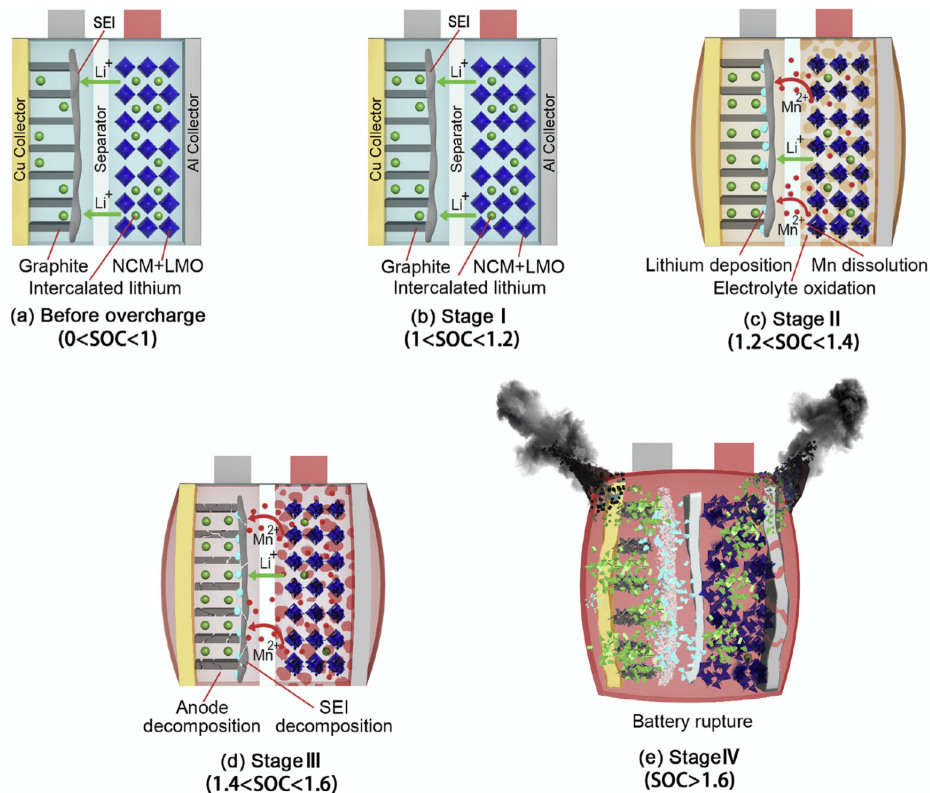


Figure 2.3: Overview of the overcharge side reactions at each stage for lithium ion batteries with NCM + LMO cathode. Source: Ren (2017) [42].

Overcharge first causes electrolyte decomposition at the cathode interface [56]. This reaction slowly increases the battery temperature. Subsequently, excessive Li⁺ deintercalation from the cathode occurs. The cathode material becomes unstable and start to release oxygen, while excess Li⁺ deposits on the anode to form Li dendrite [57]. Heat and gas generation during the side reactions would lead to safety accidents, such as cell overheating and rupture [58].

The principle of over-discharge is similar that of overcharge. Some cells reach the set state

of discharge (SOD) in advance. Thus, an over-discharge occurs if a cell is forced to continue to discharge [59]. Forced over-discharge continuously releases Li⁺ from the anode, which change the graphite structure and destroy the SEI. At very deep SOD, a copper current collector is oxidized, with the released copper ions potentially being deposited on the cathode surface [60]. Too much copper deposition results in the short-circuit of cell.

- **Overcharge/over-discharge tests** are intended to assess processes that occur in a cell when the charge or discharge processes are out of control. According to the IEC standard test, the cell is first discharged to 3.0 V, and then is charged under 10 V. If the battery does not combust or explode during or after the test it is considered safe, its materials (electrolyte, active electrode materials, separators etc.) are regarded as having adequate properties, and the structural design is deemed satisfactory. The safety performance under overcharge is closely related to the charge rate, so overcharging is performed at different rates to establish at which extreme rate and voltage failure occurs [32].
- **Internal short circuit (ISC) tests** assess the short circuiting that is caused by internal electrical connections of battery poles under abnormal conditions. Several methods are used to initiate an internal short circuit, including nail penetration, heavy impact, crush and forced ISC [32].
- **External short circuit tests** assess the short circuiting that is caused by external electrical connections of battery poles under abnormal conditions. According to the GB31485-2015 procedure, the battery is kept at 25 ± 2 °C in a fully charged state for 30 minutes, then the cathode and anode terminals are connected with a wire, and the external resistance is kept at 5 mΩ. During this test, the temperature and voltage are monitored simultaneously, throughout the entire test. The test is considered successful if the cell does not explode or combust [32].

Mechanical Abuse Tests

Due to the high energy density of LIBs, local damage caused by external influences, for example in case of EV collisions, will release a significant amount of heat, which can easily cause thermal runaway. As a result their failure risk is high. As the number of EVs (containing LIBs) on the roads continues to increase, safety concerns over battery behavior during potential vehicle collisions are becoming more prominent [32].

Mechanical abuse tests are conducted in order to assess LIB safety under mechanical abuse conditions (e.g. crushing, penetration, and vibration) that may occur during battery production, transportation, and use.

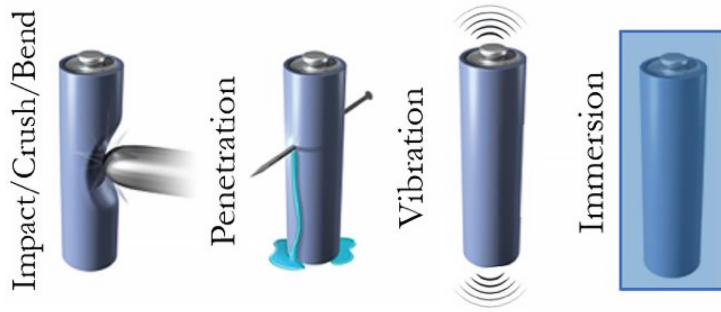


Figure 2.4: Illustration of various mechanical abuse mechanisms. Source: Fransson (2024) [61].

Nail penetration tests are the most common type of mechanical tests, and they are designed to simulate internal battery short circuits arising when a battery's internal membrane is penetrated by impurities. According to GB/T 31485, a fully-charged battery should be penetrated with a high temperature-resistant steel spike of $\varphi 5\sim8$ mm in a direction perpendicular to the polar plate at a speed of 25 ± 5 mm/s. The penetration position should also be close to the geometric center of the penetrated surface, with the steel spike retained inside the battery. The test is considered successful if the cell does not explode or combust [32].

Thermal Abuse Tests

In thermal abuse situations, a battery experiences thermal shock, or its local temperature is too high [62]. In theory, battery cycling cannot cause safety accidents because the heat generated during normal anodic and cathodic reactions is insufficient to cause a sharp temperature increase. In reality, however, the electrode heat release rate is often higher than its cooling rate. Heat dissipation of a LIB depends on its external surface area and geometry. Heat dissipation by radiation helps to alleviate some of the generated heat. As a result, some of the heat remains stored inside the battery. At some point, if this heat continues to accumulate instead of being dissipated, exothermic side reactions start to occur, further concentrating thermal stress [63].

Heating tests assess the thermal runaway caused by a battery being heated due to local overheating, and the subsequent thermal runaway expansion. Heating is used to analyze LIBs' thermal stability and heat distribution to ensure they have sufficiently efficient heat management and capability to forecast potential hazards. The results are then used to assess how thermal abuse consequences can be alleviated. Specifically, data obtained from hot box experiments are used to simulate their thermal characteristics, allowing to assess possible improvements in their design, materials and cooling systems [32].

2.2.2. Hazard level

In evaluations of batteries' safety condition based on results of the above abuse tests, the EUCAR Hazard Levels [64] and the associated criteria that are widely applied. Typically, hazard levels of Electrical Energy Storage System (EESS) devices according to their responses to abuse conditions are assigned by EUCAR and presented in Table 2.3. Manufacturers and integrators may find it helpful and useful to take these levels into consideration when evaluating a given EESS design's abuse response.

Hazard Level	Description	Classification Criteria & Effect
0	No effect	No effect. No loss of functionality.
1	Passive protection activated	No defect; no leakage; no venting, fire or flame; no rupture; no explosion; no exothermic reaction or thermal runaway. Cell reversibly damaged. Repair of protection device needed.
2	Defect/Damage	No leakage; no venting, fire or flame; no rupture; no explosion; no exothermic reaction or thermal runaway. Cell irreversibly damaged. Repair needed.
3	Leakage (Δ mass < 50%)	No venting, fire or flame; no rupture; no explosion. Weight loss < 50% of electrolyte weight (electrolyte = solvent + salt).
4	Venting (Δ mass \geq 50%)	No fire or flame; no rupture; no explosion. Weight loss \geq 50% of electrolyte weight (electrolyte = solvent + salt).
5	Fire or Flame	No rupture; no explosion (i.e. no flying parts).
6	Rupture	No explosion, but flying parts of the active mass.
7	Explosion	Explosion (i.e. disintegration of the cell).

Table 2.3: EUCAR hazard levels and associated criteria. Source: EUCAR (2019) [64].

2.3. Safety Features in Commercial Batteries

Battery safety is dependent on the nature of the active materials and the electrolyte used, how quickly heat is generated and removed, and the capacity to endure external forces. Initially, safety assessments should concentrate on examining the electrode active materials, electrolytes, and separators since these elements are the most manageable. Conversely, it's also crucial to engineer strategies that mitigate the effects of thermal and electrical abuse within lithium-ion batteries. Additionally, testing newly produced LIBs for safety before their integration into devices is a vital step.

Given that the primary causes of safety incidents in LIBs stem from unwanted and uncontrollable heat and gas produced by various side reactions, enhancing battery safety should

prioritize methods that prevent excessive heat generation, maintain operation within an optimal voltage range, and enhance cooling efficiencies. This can be done by two methods, one by avoiding operation conditions, which lead to heat and gas formation, the other being the process to control the heat and gas formation to avoid failure [32].

Enhancing the stability of lithium-ion batteries (LiBs) can be achieved through modifications in the battery's chemistry or structure, specifically in the electrodes and electrolytes. One approach includes adding fire-retardant additives to electrolytes, which are non-flammable and prevent the spread of heat-producing reactions. Another strategy involves limiting current flow during operation by using devices like PTC (Positive Temperature Coefficient) thermistors, which react to temperature changes to control current. Incorporating safety mechanisms directly into the battery design, such as vents, fuses, and additives that interrupt current in emergencies, also helps maintain safety without compromising the battery's size or cost. Thermal management is essential to avoid dangerous overheating, with methods ranging from air and liquid cooling to phase change materials for extreme conditions. In the event of a fire, electric vehicles use various extinguishing agents, like water, water mist, and halons, often enhanced with additives, to effectively combat fires caused by battery failures [65].

3 | Synchrotron X-Ray Imaging

Lithium-ion batteries are closed systems with complicated internal structures. To improve their performance, it is necessary to use many characterization techniques to check and understand the internal changes during charge, discharge and abuse tests. The synchrotron-based X-ray techniques provide powerful tools for studying and monitoring the changes of crystal structure, electronic structure, chemical composition, and morphology of electrode materials in electrochemical cells during operation, and the results are very valuable to improve the performance of existing systems and to design new battery materials [66, 67, 68, 36, 69]. High-brilliance synchrotron X-ray sources offer opportunities to perform *in situ*/*operando* experiments with various techniques to study dynamic properties and time-dependent reaction process.

The key benefits of using *in situ*/*operando* techniques compared to *ex situ* methods for characterizing materials include:

1. *In situ* measurements offer direct observation of events at specific locations within a sample, leading to more accurate and reliable data;
2. *Operando* measurements allow for the continuous monitoring of electrochemical, physical, or chemical changes in a single sample or device under actual operating conditions, thereby avoiding the need for preparing multiple samples for *ex situ* analysis and offering information that is closer to real-time;
3. These techniques enable the study of dynamic or rapid processes and the detection of transient states or intermediate species that *ex situ* methods might miss;
4. *In situ* approaches also prevent contamination, structural relaxation, or irreversible changes in highly reactive samples during preparation, handling, and transfer for *ex situ* analysis, ensuring that true reaction products are more accurately identified.

In light of these advantages, ID19 at the European Synchrotron Radiation Facility is actively conducting *in situ*/*operando* computed tomography (CT) experiments to study lithium-ion batteries under abuse conditions. This technique is particularly useful for studying the internal structure of batteries, as it can be used to monitor the changes in

the electrode materials during charge, discharge, and abuse tests. This chapter provides an overview of the experimental setup for *in situ*/*operando* experiments at ID19 and describes the CT technique and its applications in battery research.

3.1. European Synchrotron Radiation Facility (ESRF)

In most X-ray imaging applications, the source is either an X-ray tube or a synchrotron storage ring. In both cases, X-rays are produced by the acceleration of electrons. Several factors give synchrotron radiation an advantage over tube sources for X-ray imaging. First, the intensity of X-rays delivered to a specimen is much greater, and synchrotron radiation can be tuned to a very narrow energy range most advantageous for examining a given sample. The relativistic character of the synchrotron radiation emission process confines the resulting radiation to directions very close to the plane of the electron orbit, and the divergence of the beam is very small. Thus, synchrotron radiation not only possesses very high flux, but it also has much higher brightness (intensity per unit area of source) [70].

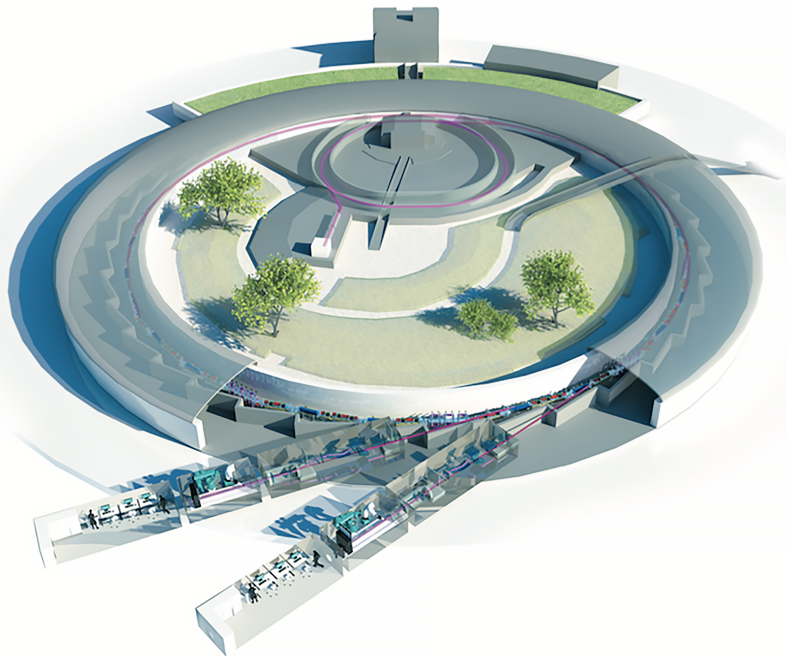


Figure 3.1: The European Synchrotron Radiation Facility (ESRF) accelerators. Source: ESRF website (2024) [71].

The European Synchrotron Radiation Facility (ESRF) is located in Grenoble, France, and it is a joint facility supported and shared by 21 countries. At time of writing, ESRF is the world's brightest X-ray source.

The accelerator complex is composed of three parts: the linear accelerator (LINAC), the booster synchrotron and the storage ring. The LINAC pre-injector accelerates electrons up to an energy of 200 MeV and transfers them to the 300-meter booster synchrotron, where they are further accelerated to an energy of 6 GeV. The electrons are then injected into the 844-meter storage ring, which is designed to store the 6 GeV electron beam and deliver it to the 42 beamlines. The beam is guided onto orbit by 128 bending magnets with a longitudinal gradient and 96 bending magnets with a transfer gradient. The beam is focused by 412 quadrupoles. 192 sextupoles control the energy dispersion of the electrons [71].

The ESRF hosts a variety of beamlines, categorized into Insertion Device (ID) beamlines and Bending Magnet (BM) beamlines, each designed for specific types of experiments and research. BM beamlines use the synchrotron radiation generated by bending magnets, offering a wide range of X-ray wavelengths for diverse scientific disciplines. ID beamlines, on the other hand, utilize insertion devices such as undulators and wigglers to produce highly brilliant and coherent X-ray beams, tailored for advanced imaging and spectroscopy applications. Among these, the ID19 beamline stands out for its versatility, allowing for a wide range of experiments (radiography, tomography and laminography) in the fields of materials science, physics, and chemistry [72].

3.1.1. Beamline ID19

The ID19 beamline is located 145 m from the storage ring and is classified as a long beamline. Five insertion devices are located in the ID19 straight section (four undulators and one wiggler), the choice of one of them as source being a function of the experiment requirements. The length of the beamline coupled with the small source size allows the exploitation of the coherence properties of the beam and the versatility of having either a wide and homogeneous beam or a focus spot below 100 nm when required. High vacuum is required to avoid scattering of low energy X-rays by gas atoms and to avoid oxidation of optical devices [72].

Before entering the experimental hutch, the beam passes the optics hutch and mono hutch (Figure 3.2) where the beam flux and brilliance can be conditioned to suit the experimental conditions. Monochromators positioned within the mono hutch enable the selection of specific wavelength ranges, attenuators can be employed to decrease the intensity of the spectrum's low energy portion, while slits are used to trim the beam's size. The beam is delivered from the optics hutch by propagation through a helium atmosphere, blocked by the safety shutter when the hutch is accessed [72].

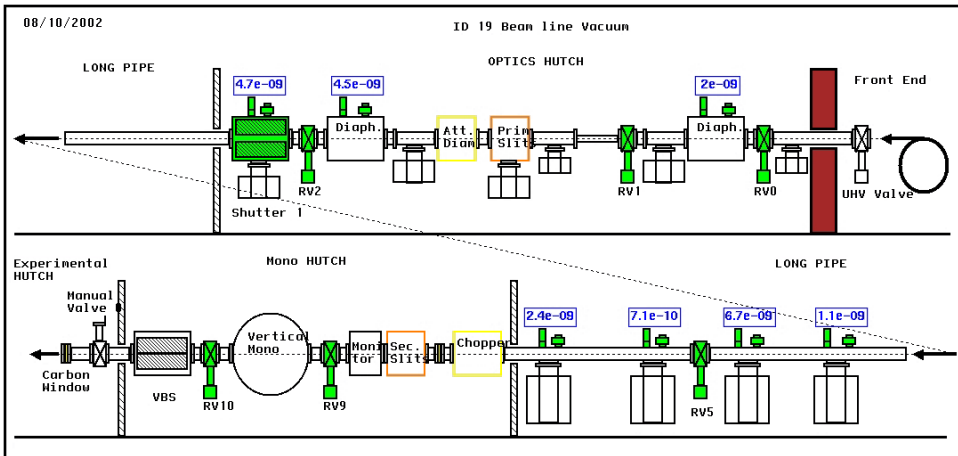


Figure 3.2: Schematic illustration of ID19 hutches and X-ray optical elements. Source: ID19 website (2024) [72].

In the experimental hutch, the sample is aligned with the beam and detector by remotely controlling high precision motors. For optimal image acquisition, indirect detectors consisting of single crystal scintillators and visible light optics arranged in a periscope design via a mirror are used. All beam delivery instruments are controlled by the inhouse-developed BLISS (BeamLine Instrumentation Support Software) [73].

3.2. X-ray Computed Tomography

X-ray computed tomography (CT) offers unparalleled insights into the internal structures of materials non-destructively, covering scales from meters to tens of nanometers. It utilizes X-rays' ability to penetrate objects, capturing multiple two-dimensional radiographs from various angles. These radiographs are then processed through a reconstruction algorithm to produce a digital greyscale three-dimensional image, or *tomogram*, showcasing the internal structure of the object (Figure 3.3). This 3D representation allows for detailed analysis and virtual manipulation, including slicing in any direction and enhancing specific features for better visualization.

A key advantage of X-ray CT is its non-destructive nature, making it indispensable for examining fragile or important samples where preserving integrity is crucial. This feature also enables longitudinal studies to track changes in 3D structures over time. When deciding how to undertake a CT scan, several important factors need to be considered, including the object size, the features of interest and their composition, the allowable dose and the temporal resolution.

The resolution of CT images is determined by the size of voxels, the 3D equivalent of pixels,

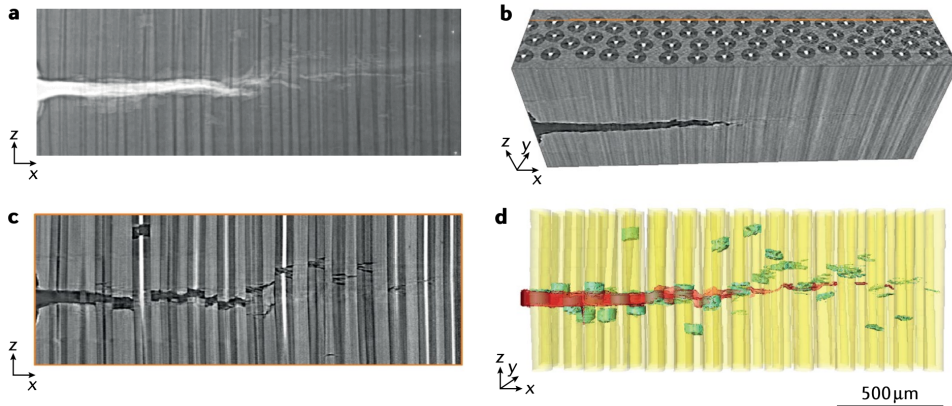


Figure 3.3: Computed tomography (CT) scan of a fatigue crack in a titanium/silicon carbide tungsten-cored monofilamentary fibre metal matrix composite imaged at maximum crack opening load. **a** | Radiograph (projection). **b** | Reconstructed tomogram. **c** | Virtual cross-section. **d** | Volume rendering showing fibres (yellow), titanium matrix (transparent), matrix crack (red) and fibre fractures (green). Source: Withers (2021) [74].

with the requirement that voxels be smaller than the features being studied. Resolutions range from sub-millimeter in conventional CT to micrometer in microCT, and down to nanometer in nanoCT. Choosing a smaller voxel size often requires compromising on the size of the object being scanned. This is due to the smaller effective pixel size leading to a reduced field of view (FoV) on the detector. Additionally, the need to combine several FoVs to cover the entire object significantly extends the acquisition time and amplifies both the computational effort needed for image reconstruction and the data storage demands, as the ratio of sample size to voxel size grows.

The contrast recorded by each projection is dependent on the interaction of X-rays with matter. As a result, two contrast modes are possible that suit different types of imaging task. When an electromagnetic X-ray wave passes through an object, both the intensity and the phase change vary according to the refractive index, n :

$$n = 1 - \delta + i\beta \quad (3.1)$$

where the imaginary part (β) controls the attenuation (absorption) and the real part (δ) the phase shift as the X-rays pass through the object. The former is exploited to obtain attenuation contrast, while the real part is exploited for phase contrast. The linear attenuation coefficient, μ , expresses the attenuation of X-rays as they pass through the material and is given by $4\pi\beta/\lambda$, where λ is the X-ray wavelength [74].

Because the illumination provided by X-ray sources is far from uniform, and detectors

show pixel to pixel variations in sensitivity, flat field correction and dark field correction are necessary to compensate for these variations during reconstruction:

$$I^{\text{corr}} = \frac{I^{\text{signal}} - I^{\text{dark}}}{I^{\text{flat}} - I^{\text{dark}}} \quad (3.2)$$

The correction is applied by subtracting the dark field I^{dark} (projection acquired with the light source turned off) to both signal I^{signal} and flat field I^{flat} (projection acquired without the sample in the FoV) prior to division.

3.2.1. Attenuation Contrast CT

In attenuation contrast CT, the contrast obtained in each projection of the object is related to the attenuation of the beam. It is given by the line integral of the attenuation arising from the material encountered on the path of the beam as it passes through the object. For an object comprising multiple ($i = 1 \dots n$) materials in the beam path, the transmitted intensity, I , falls exponentially compared with the incident intensity, I_0 , and is described by Lambert-Beer's law:

$$I = I_0 e^{-\sum_{i=1}^n \mu_i x_i} \quad (3.3)$$

where μ_i and x_i are the linear attenuation coefficient of, and the path length through, the material i . Each reconstructed slice is a map of the linear attenuation coefficient $\mu(x, y, z)$ for the corresponding section in the object. Contrast sensitivity, which is the extent to which small changes $\Delta\mu$ can be detected, and resolving power, which is the degree to which small, closely spaced features can be distinguished, depend on CT instrument, the sample and the data acquisition parameters. Materials having similar atomic numbers (Z) tend to produce little absorption contrast.

The dependence of the linear attenuation coefficient (μ) of a given element on X-ray energy is smooth except for step changes that occur at the characteristic absorption edges. As μ changes abruptly at the element-specific energies corresponding to these edges, they can be used to enhance contrast in X-ray CT or to identify the presence of different elements. In synchrotron source CT, one can optimize contrast from element Z by collecting projection sets at energies on either side of a characteristic absorption edge of Z. Numerical comparison of the pairs of reconstructions shows where element Z is concentrated.

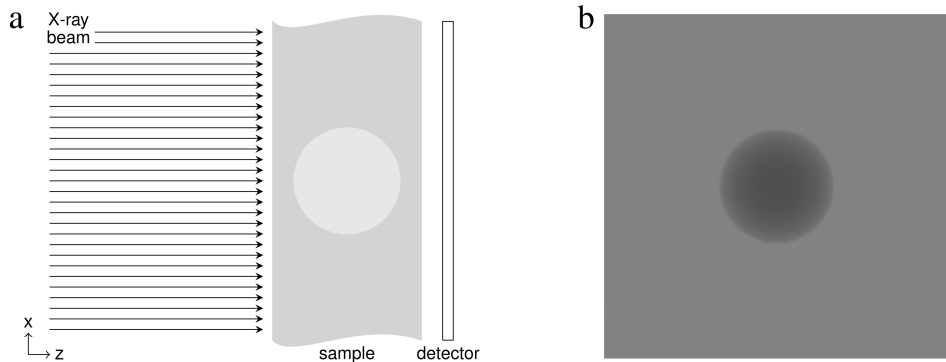


Figure 3.4: **a** | Simple model for the generation of contrast in absorption-based X-ray imaging. **b** | Corresponding image recorded represented as the two dimensional distribution of intensity. Source: Endrizzi (2018) [75].

3.2.2. Phase Contrast CT

While attenuation contrast is effective for imaging objects made of vastly different materials (since the linear attenuation coefficient typically increases sharply with atomic number), many specimens contain materials with similar attenuation characteristics (such as soft tissues), and enhanced contrast can be achieved by utilizing the materials' X-ray phase contrast (Figure 3.5).

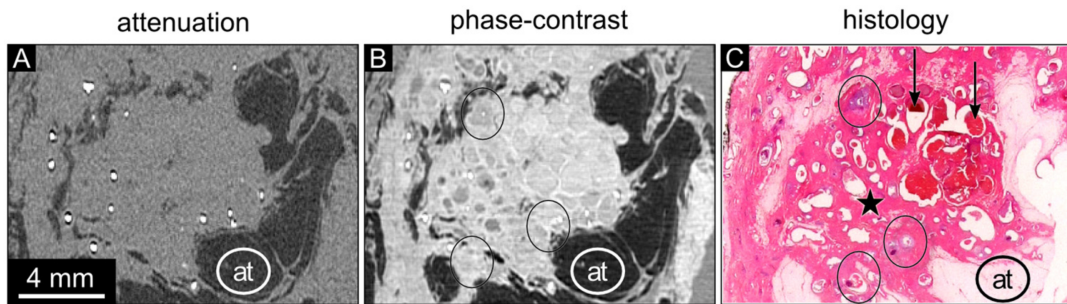


Figure 3.5: Attenuation contrast (**a**), phase contrast (**b**) and histology (**c**) images of breast tissue. Source: Hellerhoff (2019) [76].

Phase contrast stems from variations in the real part (δ) of the refractive index (Equation 3.1), which generates a phase shift in the propagating X-ray wavefront, rather than the imaginary part (β), which describes the attenuation. For weakly attenuating materials and within the lower X-ray energy regime, δ can be orders of magnitude larger than β . As a result, greater contrast can be expected by designing the imaging process to detect phase shifts and by incorporating their extraction into the reconstruction step. Phase shifts are detected indirectly by measuring modulated intensity patterns because

direct measurement of the phase of an electromagnetic wave at optical frequencies and above is not possible. Several different experimental approaches exist for detecting phase shifts: interferometry, propagation based imaging, analyzer based imaging, grating based imaging and tracking based methods. The simplest approach (and also the one used at ID19) is propagation-based imaging, whose set-up is identical to that of a conventional CT apparatus except that propagation distance R_2 between the sample and the image receptor is sufficiently large to make phase effects detectable. The X-ray wave passes through the specimen and propagates in space before its intensity is recorded; parts of the wave with different phases interfere, modulating the intensity and producing intensity peaks and troughs at internal and external boundaries.

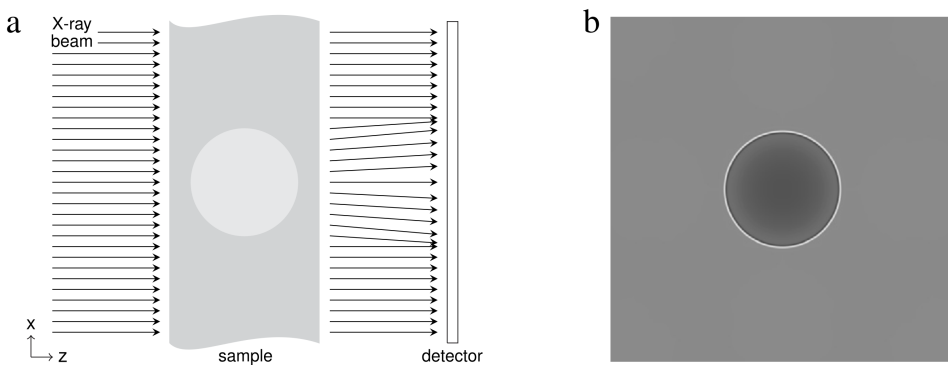


Figure 3.6: **a** | Simple model for the generation of a phase contrast image with the free space propagation technique. **b** | Corresponding image recorded represented as the two dimensional distribution of intensity. Source: Endrizzi (2018) [75].

This phenomenon can be interpreted in terms of Fresnel diffraction and key features of this approach to imaging can be identified by referring to the expression that describes the intensity distribution at the image receptor plane from a pure phase object [75]:

$$I(x, y, \lambda) = I_0 \left[1 + \frac{R_2 \lambda}{2\pi} \nabla_{\perp}^2 \phi(x, y, \lambda) \right] \quad (3.4)$$

where λ is the X-ray wavelength, I_0 is the light intensity before it interacts with the sample, R_2 is the distance between the sample and the detector and $\nabla_{\perp}^2 \phi(x, y, \lambda)$ is the Laplacian of the phase function.

Another feature of interest is that the monochromaticity of the radiation is not essential for this type of imaging. A necessary condition, however, is that the radiation must have a certain degree of spatial coherence. The coherence length l_c has to be comparable to or larger than the inverse spatial frequency of the feature of interest in order to obtain

significant phase contrast. In practice this means that the source has to be relatively small or that the object must be placed at a relatively large distance R_1 from it. Since the sample is placed at a distance of at least 145 m from the source at ID19, the coherence length is sufficient to obtain phase contrast.

The intensity projection image, acquired with a certain propagation distance between the sample and the detector, will contain a mixture of contributions from both the absorption and the phase shifts in the sample. Other experimental parameters, like the X-ray energy, the geometrical magnification, the radiation coherence and the system resolution, determine the modulation of intensity at the detector. The process that aims at making this type of imaging quantitative by calculating phase and amplitude at the exit surface of the sample is called phase retrieval.

3.2.3. Reconstruction Algorithms

Computational reconstruction recovers the spatial distribution of the object function $f(x, y)$ (which corresponds to either the attenuation coefficient $\mu(x, y)$ in the case of absorption contrast, or the phase decrement $\delta(x, y)$ for phase contrast) slice by slice, from the set of projections (radiographs). The relationship between the slices and projections is described mathematically by the Radon transform. Two broad classes of reconstruction algorithms, namely analytic and iterative methods, are based on the transform. The filtered backprojection (FBP) algorithm is an analytic, fast and robust method based on the Fourier slice theorem, and is the most commonly used algorithm in CT.

In the context of propagation-based phase contrast X-ray tomography, an additional pre-processing step is crucial for enhancing the contrast of the reconstructed images by accounting for phase effects inherent to the imaging technique. This step involves the application of a Paganin filter [77] to the radiographic projections prior to reconstruction.

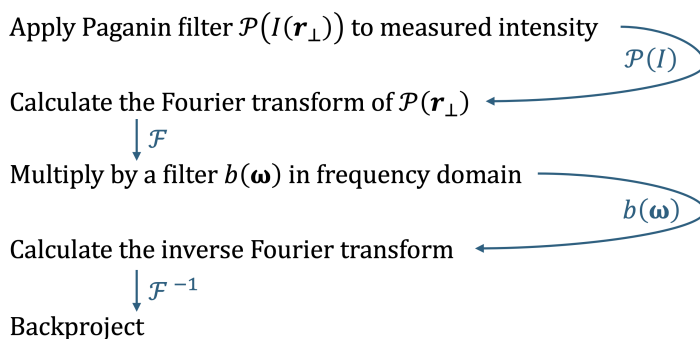


Figure 3.7: Paganin filtering and filtered backprojection (FBP) reconstruction algorithm. Adapted from: Burvall (2011) [78].

The Paganin filter is a method for the extraction of a contrast-enhanced contact absorption image ($z = 0$) using a single propagation-induced phase contrast image ($z = R_2$).

The derivation of the filter is based on two assumptions:

1. **Monochromatic beam:** The X-ray beam is assumed to be monochromatic. In practice, the loss of contrast due to polychromaticity is negligible for most applications. This is because the filter's effectiveness in enhancing contrast by compensating for phase shifts is not significantly diminished by the slight variations in attenuation that polychromatic X-rays might introduce.
2. **Homogeneous object:** The object is assumed to be homogeneous and the phase shift to be proportional to the attenuation coefficient. This assumption is pivotal for the successful application of the filter, as it supports the mathematical model that relates phase shifts to observable intensity changes in the X-ray image. Having multiple materials with different attenuation coefficients would cause at least some of them to be blurry or noisy in the reconstructed image. The larger the difference in densities between the materials, the more pronounced the effect.

The expression for the Paganin filter is given by Equation 3.5 [77]:

$$\frac{I(\mathbf{r}_\perp, z = 0)}{I^{in}} = \mathcal{F}^{-1} \left\{ \mu \frac{\mathcal{F}\{I(\mathbf{r}_\perp, z = R_2)\}/I^{in}}{R_2 \delta |\mathbf{k}_\perp|^2 + \mu} \right\} \quad (3.5)$$

where \mathcal{F} and \mathcal{F}^{-1} are the Fourier transform and its inverse, $I(\mathbf{r}_\perp, z = 0)$ and $I(\mathbf{r}_\perp, z = R_2)$ are the intensity distributions at the detector plane at the sample and at the propagation distance R_2 , I^{in} is the incident intensity, μ is the linear attenuation coefficient, δ is the phase decrement, and \mathbf{k}_\perp is the spatial frequency vector in the plane perpendicular to the beam direction.

Once the Paganin filter has been applied to the projections, the filtered projections are reconstructed using the FBP algorithm, which can be divided in three essential steps: the Radon transform relating the desired object function $f(x, y)$ with the experimental set of projections, the Fourier slice theorem relating the one-dimensional Fourier transform of the projection with the two-dimensional Fourier transform of $f(x, y)$, and the FBP correcting for data blur.

For one angle θ , the projection can be related to the object function $f(x, y)$ as [79]:

$$\begin{aligned} p_\theta(r) &= \mathcal{R}_\theta \{ f(x, y) \} \\ &= \int_0^d f(r, s) ds \\ &= \iint_{-\infty}^{\infty} f(x, y) \delta(x \cos \theta - y \sin \theta - r) dx dy \end{aligned} \quad (3.6)$$

where δ is the delta distribution and the polar coordinates are defined as $r = x \cos(\theta) - y \sin(\theta)$ and $s = x \sin(\theta) + y \cos(\theta)$ (Figure 3.8).

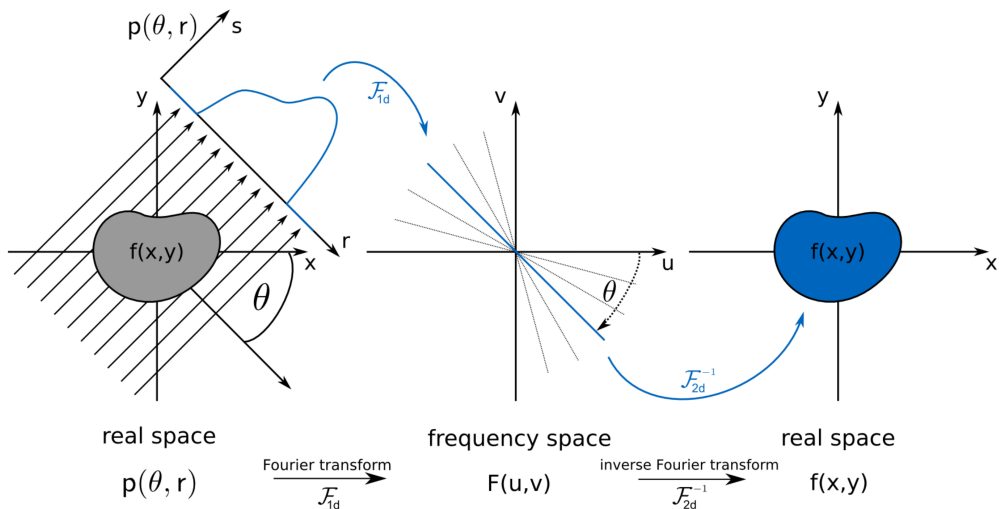


Figure 3.8: The object function is projected in beam direction forming the line integral $p(\theta, r)$. The Fourier slice theorem states that the one-dimensional Fourier transform of a single projection $p(\theta, r)$ corresponds to a slice of the two-dimensional Fourier transform of the object function under the same angle θ . If the two-dimensional Fourier transform is sampled, the object function $f(x, y)$ is determined via two-dimensional inverse Fourier transform. Source: Birnbacher (2019) [79].

At this point, by applying simple backprojection (i.e. inverting the Radon function), one could retrieve the object function $f(x, y)$ from the projections. However, this process turns out to blur the reconstructed data. One view to this issue is illustrated in the frequency representation after two-dimensional Fourier transform in Figure 3.9.

The sampling is higher in the center at low frequencies than for higher frequencies in the outer region, so the distance between two points increases with higher frequencies. For all frequencies to be equally represented, the distance between all sampling points should be the same.

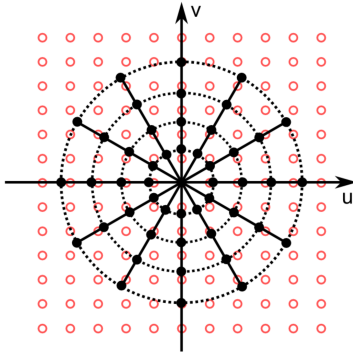


Figure 3.9: Radial frequency distribution of the experimental data. Source: Birnbacher (2019) [79].

The solution for being fast, not interpolating in frequency space, and filtering efficiently is the filtered backprojection. The idea is to calculate the one-dimensional Fourier transform of a line integral, multiply with a filter function correcting for the blur, calculate the one-dimensional inverse Fourier transform, and perform the backprojection.

The Fourier slices theorem or central slice theorem states that a one-dimensional Fourier transform of a projection $p(\theta, r)$ equals a slice of the two-dimensional Fourier transform of the object $f(x, y)$ under the same angle. The one-dimensional Fourier transform of the projection is then [79]:

$$\begin{aligned} P(\theta, \omega) &= \mathcal{F}_{1D} \{ p(\theta, r) \} \\ &= \mathcal{F}_{2D} \{ f(x, y) \} \\ &= F(u = \omega \cos \theta, v = -\omega \sin \theta) \end{aligned} \tag{3.7}$$

with $F(u, v)$ being the two-dimensional Fourier transform of $f(x, y)$ and $u = \omega \cos \theta$ and $v = -\omega \sin \theta$ being the Cartesian Fourier frequencies. The Fourier slice theorem legitimates us to calculate the respective one-dimensional Fourier transforms of the line integrals, instead of the two-dimensional Fourier transform of the object function.

The filtered backprojection is now the inverse process from the experimentally determined projections $p(\theta, r)$ to the object function $f(x, y)$ with the use of the Fourier slice theorem. The object function can be expressed as an inverse Fourier transform [79]:

$$\begin{aligned} f(x, y) &= \iint_{-\infty}^{\infty} F(u, v) e^{2\pi i(ux+vy)} du dv \\ &= \int_0^\pi \int_{-\infty}^{\infty} P(\theta, \omega) |\omega| e^{2\pi i\omega(x \cos \theta - y \sin \theta)} d\omega d\theta \end{aligned} \tag{3.8}$$

The factor $|\omega|$ is called Ram-Lak filter and corrects low frequency data blur. There exist however different modifications of this filter accounting for CT typical characteristics like noise and spatial resolution like the Cosine ($|\omega| \cos \pi\omega$), Hann ($|\omega| [0.5 + 0.5 \cos 2\pi\omega]$), or Shepp-Logan filter ($|\sin \omega|$).

By way of example, consider parallel beam CT of an object (here, a human head), as depicted in Figure 3.10. If we consider one cross-sectional slice, recorded by a row of pixels on the detector, we can represent the attenuation as a line profile. For a given projection angle, θ , each pixel on the detector sums the X-ray photons passing through the specimen slice along a given beam path; Figure 3.10b shows three projection angles and the corresponding projection (a line profile) of absorptivity.

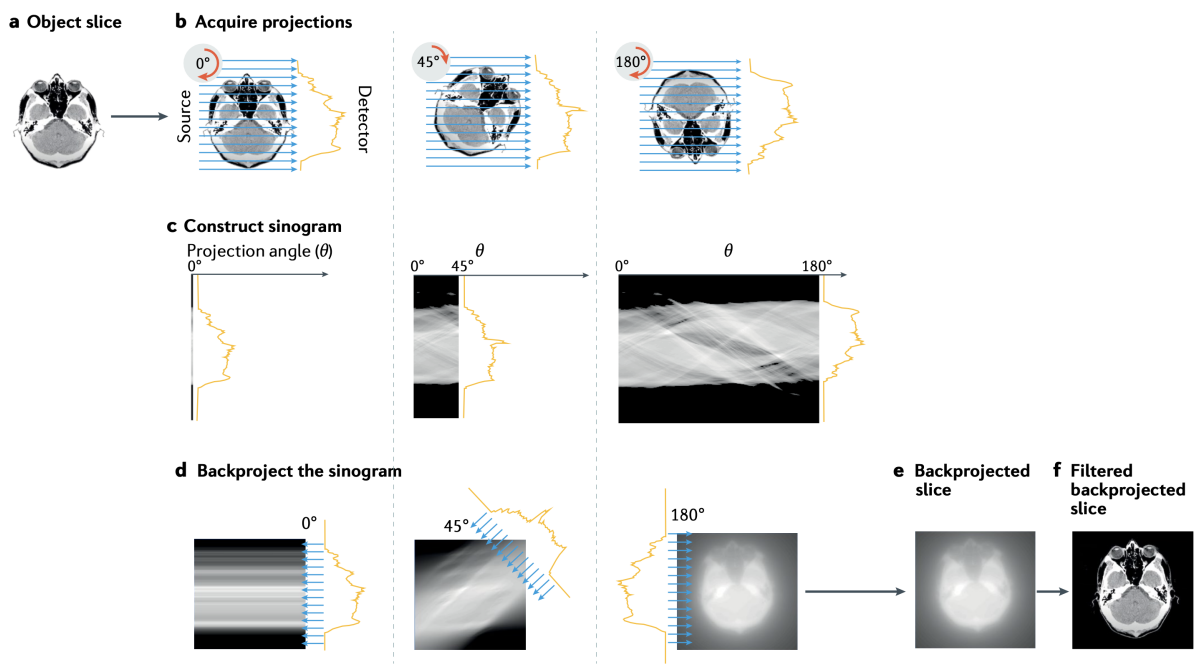


Figure 3.10: Backprojection reconstruction method for a single slice obtained by parallel beam computed tomography. **a** | Original object slice (a human head where the highly attenuating features are brightest). **b** | Set of projections collected at different angles. **c** | Sinogram resulting from many projections. **d** | Process of backprojecting the sinogram. **e** | Final backprojected image. **f** | Equivalent filtered backprojection image. Note that with fewer projections, the image quality would decrease. Source: Withers [74].

As the sample is rotated, the row of pixels traces out a sinogram (Figure 3.10c) showing the variation in attenuation across the row of pixels as the projection angle varies. In Figure 3.10d, the backprojection reconstruction algorithm takes each projection making up the sinogram and mathematically projects it back along the angle θ at which it was recorded. With an increasing number of line profiles (corresponding to an increasing

number of radiographs) backprojected, an increasingly faithful backprojection image of the object is recovered. However, it is evident from Figure 3.10d that backprojection spreads mass where there is, in fact, no mass, introducing blurring into the reconstruction (as seen by comparing Figure 3.10a and Figure 3.10e). FBP corrects for this blurring by applying a filter to the projections. This suppresses the low frequencies to compensate for the high-frequency components in Fourier space that are missing (due to insufficient sampling) and leads to a sharper image (Figure 3.10f).

An important question to ask is how many projections are required to recover an acceptable image. At a minimum, the angular change between projections should be no greater than the voxel size at the outer diameter of the object. Therefore, the number of points needed along the circumference to satisfy the sampling condition is $q\pi$, where q is the number of pixels across the diameter of the object. As each projection profile provides two points along this circumference, the minimum number of projections is $q\pi/2$, which is in line with more rigorous analyses. When the number of projections is too sparse or non-uniform, then imaging artefacts will occur.

3.3. High-speed Lithium-ion Battery Tomography

The high-speed X-ray imaging setup employed at ID19 was developed through a collaboration between the European Synchrotron Radiation Facility (ESRF), the Fraunhofer Institute for High-Speed Dynamics (Ernst-Mach-Institut, EMI), and University College London (UCL). The following section provides a detailed description of the experimental setup used in the July 2022 experiments, the data from which I have analyzed throughout the course of my thesis.

To perform battery abuse test at the synchrotron, a specialized X-ray penetrable chamber has been developed and installed at the beamline (Figure 3.11). The chamber provides the capability to robustly perform *in situ* abuse tests through the heat-resistant and gas-tight design for flexible battery geometries and configurations, including single-cell and multi-cell assemblies. High-speed X-ray imaging can be complemented by supplementary equipment, including additional probes (voltage, pressure and temperature) and thermal imaging. The propagation distance of 8 m between the battery abuse test chamber and the detector allows for the detection of phase contrast. The chamber is equipped with a high-speed sample rotation stage (20 Hz) and compatible sample holders for different battery types. A more detailed description, application settings and parameters for the synchrotron adapted battery abuse test chamber can be found in [80].

The X-ray beam was tuned to 85 keV with a wiggler gap of 26.5 mm and filtered by the

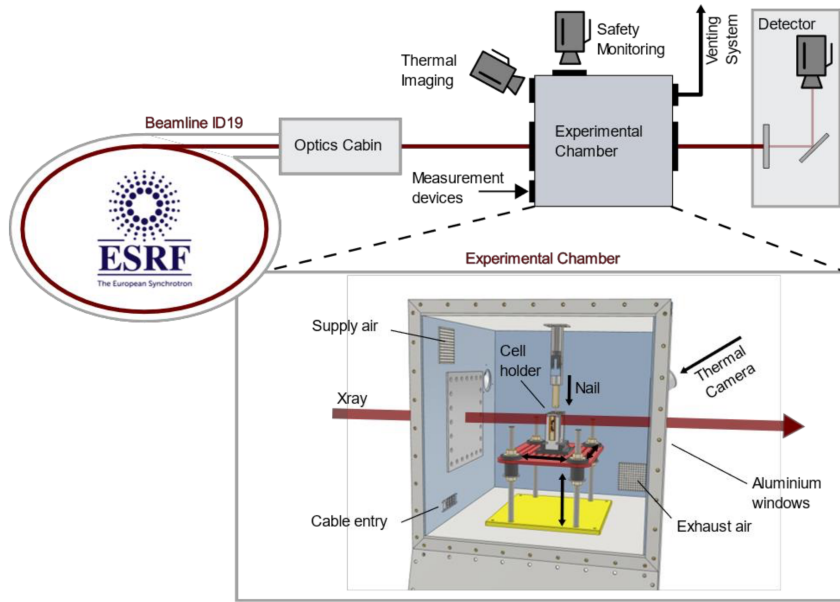


Figure 3.11: High-speed X-ray imaging setup for battery abuse tests at the European Synchrotron Radiation Facility. Source: Pfaff (2023) [80].

attenuators (5.2 mm Al, 3.8 mm Cu) and the aluminium windows of the rig.

A horizontal field of view (FoV) of 40 mm was required for imaging the whole section of the battery and, possibly, sidewall ruptures, and a pixel size smaller than $40 \mu\text{m}$ was needed to resolve the internal structure of the battery. In addition, a fast detector is necessary to capture a sufficient amount of projections for satisfactory CT reconstructions. This was achieved by using a Photron SA-Z CMOS camera with a 1024×512 pixel matrix and $20 \mu\text{m}$ detector pixel size that, coupled with a tandem configuration of lenses yielding $0.5 \times$ magnification (100mm and 210mm Hasselblad optical lenses), provided a 40 mm horizontal FoV and a $40 \mu\text{m}$ pixel size.

To achieve satisfactory CT reconstructions at high speed, the sample should move no more than the pixel size Δ during the acquisition of a single projection. This criterion ensures that motion blur is minimized and the spatial resolution of the reconstructed images is maintained. Given this, the minimum frequency f_{scan} at which projections should be acquired can be determined based on the angular velocity ω of the sample stage, the radius r of the rotation, and the pixel size Δ . The tangential velocity of the battery casing v_t is related to the rotational frequency f_{rot} and the radius r of the battery, with $\omega = 2\pi f_{\text{rot}}$ representing the angular velocity. Therefore, the distance covered by a point on the external shell per scan, dx , is given by the product of v_t and t_{scan} , which is equivalently expressed as $\omega r / f_{\text{scan}}$. To prevent the target from moving more than one pixel size Δ during a single projection capture, we set $\Delta > dx$, leading to the inequality:

$$f_{\text{scan}} > \frac{\omega r}{\Delta} = \frac{2\pi f_{\text{rot}} r}{\Delta} \quad (3.9)$$

By substituting the values for f_{rot} (20 Hz, the rotation speed of the sample stage), r (9.3 mm, the maximum radius of the battery casing), and Δ (40 μm , the pixel size), the minimum frequency of $f_{\text{scan}} > 2.92 \cdot 10^4$ Hz is obtained. The acquisition frequency of the Photron SA-Z camera was set to 30 kHz to satisfy this requirement. Since reconstructions were performed each 180 degrees, 750 projections per CT were acquired, resulting in a temporal resolution of 40 CT/s.

Three different TR initiation modes (nail penetration, external heating, and internal short circuit device) were employed in this work. The speed of the nail is set to 6 mm/s with a 1 mm intrusion depth. The heat gun reaches a temperature of 800 °C and is used also for triggering the ISC failures by melting an electrically conductive wax layer. Two battery models, Molicel INR-18650-P28A 2800 mAh (which will be referred to as P28A) and Sony Murata US-18650-VTC5A 2600 mAh (which will be referred to as VCT5A), were each subjected to nail penetration and external heating, whereas Molicel INR-18650-P28B 2800 mAh (which will be referred to as P28B) was subjected to ISC.

The data was acquired as 12-bit greyscale TIFF 1024×512 images. These were cropped 640×280 because of the limited beam size of 12 mm in the vertical direction and battery diameter of no more than 20 mm the in horizontal direction (equivalent to 300 and 500 pixels, respectively, for 40 μm pixel size). The 640×640×280 volumes were reconstructed using Nabu [81]. Each dataset consists of 223 reconstructed CT volumes with a time frequency of 0.025 s (5.575 s of data acquisition), corresponding to approximately 95.3 GB of data. The volumes were converted from TIFF file collections to NumPy volumes and stored in .npy format for further analysis.

4 | Developed Software

A preliminary analysis of the reconstructed volumes has highlighted the formation of copper agglomerates as a critical event during thermal runaway. These agglomerates originate from the melting of the copper current collector, a consequence of the intense heat generation during thermal runaway. The presence and characteristics of these agglomerates are of significant interest for several reasons. Firstly, they provide valuable insights into the mechanisms of thermal runaway. By understanding the conditions under which copper melts and agglomerates form, researchers can infer critical aspects of the heat generation and dissipation processes within the battery. Secondly, the size, distribution, and morphology of these agglomerates can inform on the severity and progression of thermal runaway, offering clues to its onset and evolution. Lastly, analyzing these features can contribute to the development of safer battery designs and the implementation of preventative measures against failure.

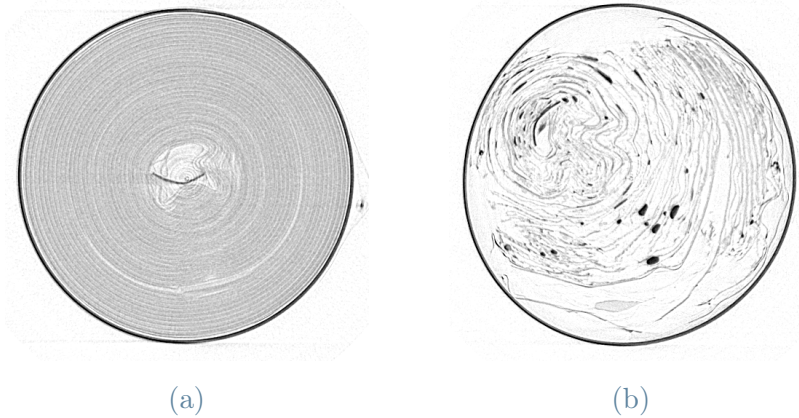


Figure 4.1: Tomography slice of a P28A battery before (a) and after (b) thermal runaway. Copper agglomerates are visible in (b). Darker areas are associated with higher absorption.

To systematically study these agglomerates, a software tool was developed aimed at segmenting and analyzing them. The software accurately identifies, segments, and characterizes copper agglomerates from the background of battery materials and artifacts inherent in tomographic imaging. The development and application of this tool are discussed in this

chapter, highlighting the algorithmic strategies employed and the challenges overcome.

4.1. Segmentation

Image segmentation is the process of partitioning an image into multiple segments or regions based on certain shared attributes, with the aim of making the image more interpretable or easier to analyze. This technique is essential for quantifying morphological characteristics within an image, facilitating tasks in computer vision, imaging, and various fields requiring detailed image analysis.

Objects in tomographic images can be grouped into regions based on voxel values. The choice of greyscale threshold is often made with reference to the image's greyscale histogram. In the idealized case (Figure 4.2), the object can easily be segmented into its component materials because the final result is relatively insensitive to the bounding greyscale threshold chosen in Figure 4.2b.

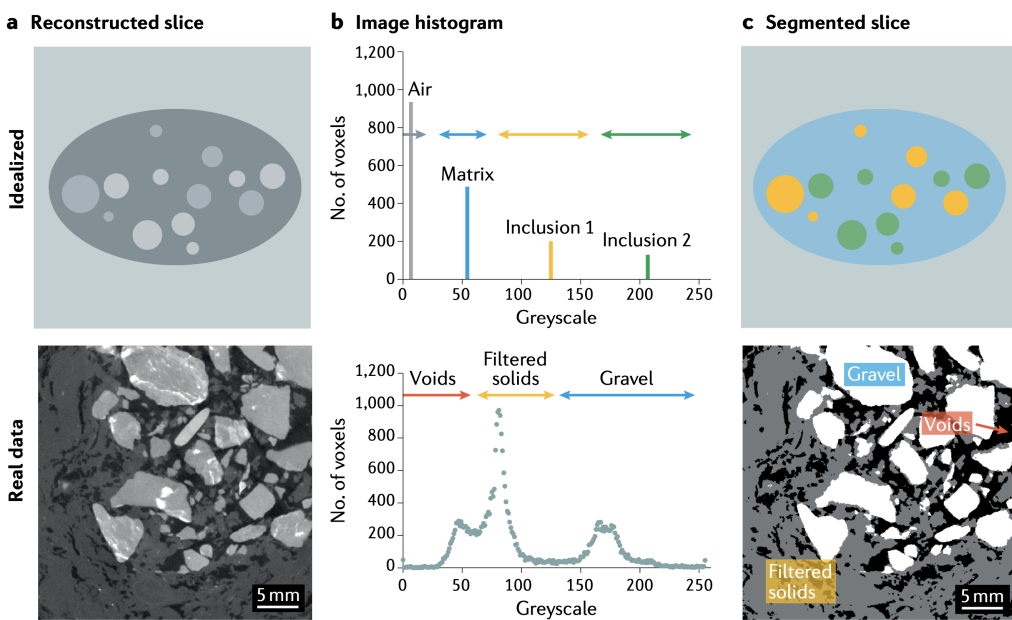


Figure 4.2: Segmentation processes for an idealized sample (top) and for a filter pack for wetland water treatment. **a** | Reconstructed tomographic slice showing different phases according to the grey levels. **b** | Greyscale histogram of the volume with the segmentation ranges used to segment the phases. **c** | Segmented slice showing the segmented regions. Source: Whitters (2021) [74].

In addition to any noise in the image, the physics of radiograph collection and artefacts from the reconstruction process lead to wide peaks in the histograms associated with the constituent phases of real specimens, and this complicates the choice of where to set the

segmentation limits. The averaging of greyscale levels in reconstructed data due to voxels containing multiple constituent materials also broadens histogram peaks. As the greyscale levels for different regions overlap, their separation based simply on greyscale thresholds is inaccurate and very sensitive to the thresholds chosen as well as to any artefacts in the image [82].

In addition to threshold-based methods, boundary-based and region-growing approaches are prominent [70]. The features present and the type of contrast dictate which method is preferable. If, for example, gradients of greyscale levels extend across the specimen owing to uneven illumination, applying a global threshold is problematic, and a local threshold method, where a variable threshold is set relative to the voxel's neighbours, works better. A powerful alternative is to segment based on a range of local greyscale gradients simultaneously with a range of greyscale levels. Boundary-based methods use relative differences in greyscale to detect the edges between materials. Watershed segmentation is a widely used region-growing method and is a direct analogue of the geographical or geological concept of a watershed: greyscale levels are considered heights and define different catchment basins. Watershed segmentation works well with foams where a significant fraction of cell walls cannot be detected.

A rapidly developing alternative to conventional methods is machine learning/deep learning for segmentation, which is most developed in medical CT image analysis [83]; typically, a neural network is trained by the investigator, with the resulting neural network being capable of automatic segmentation of large image data sets. While these methods have shown great promise in enhancing segmentation accuracy, they come with significant challenges. Chief among these is the requirement for extensive labeled datasets to train the models effectively. Neural networks like U-Net [84] rely heavily on such labeled datasets to learn the complex patterns necessary for accurate segmentation. Even semi-supervised learning methods such as variational autoencoders [85], which can leverage unlabeled data to some extent, still require a substantial amount of labeled data to achieve reliable performance.

Given the context of segmenting copper agglomerates in LIBs, the absence of a labeled dataset rendered the use of machine learning methods impractical. Consequently, after evaluating and testing the potential benefits and limitations of various segmentation techniques, a threshold-based method was chosen. Thresholding offers a straightforward yet effective approach to segmentation, particularly suited to this dataset's characteristics. Noise in the reconstructed images was minimal, and the greyscale levels of the agglomerates were distinct from those of the background materials. Furthermore, any reconstruction artefacts that could potentially affect the segmentation process were mit-

igated through the use of morphological operations and filtering. The threshold-based method is also computationally efficient, making it suitable for processing large volumes of data.

The segmentation algorithm developed for this study [86] integrates thresholding, morphological operations (erosion and dilation), and filtering techniques. Implemented in Python, this algorithm leverages the `NumPy` and `scikit-image` libraries to process reconstructed battery volumes, transforming the input data `ct` into a label map `mask`.

Input `ct` is a `NumPy` array of reconstructed volumes with the shape (223, 280, 640, 640), corresponding to the dimensions (`t`, `z`, `y`, `x`). The number `T` of reconstructed volumes per experiment is 223, and each volume comprises $640 \times 640 \times 280$ voxels. This array uses the `numpy.half` data format to efficiently store 16-bit floating-point numbers, balancing precision and memory usage.

Output `mask` is a `NumPy` array of the same shape as `ct`, containing a multi-label map. Here, 0 denotes the background, 1 indicates the battery casing and integers greater than 1 identify copper agglomerates. This map employs the `numpy.ushort` format, utilizing 16-bit unsigned integers to accomodate the range of labels required.

Algorithm 4.1 Segmentation algorithm outline.

```

1: Compute threshold
2: Segment ct[0]
3: i = 1
4: while i < T do
5:   Segment ct[i]
6:   Propagate labels from mask[i-1] to mask[i]
7:   i = i + 1
8: end while
9: Filter mask
```

Algorithm 4.1 outlines the segmentation process, which is built around four primary functions: threshold computation, segmentation, label propagation, and filtering. Initially, the algorithm calculates a threshold value for segmenting the volumes `ct[i]`. Using this threshold, the first volume is segmented to produce an initial label map `mask[0]`. For subsequent volumes `ct[i]`, the algorithm computes `mask[i]` and propagates labels from `mask[i-1]` to ensure continuity of agglomerate identification across volumes. The final step involves applying filtering techniques to the label map to refine segmentation quality and eliminate artifacts. Detailed explanations of these steps are provided in the following sections, underscoring their significance in achieving accurate and consistent segmentation outcomes.

4.1.1. Threshold computation

To accurately compute the threshold for each experiment, a dynamic approach is adopted, reflecting the variability in grayscale values due to differences in imaging conditions across experiments. Given the uniform dimensions of the battery casing in both the Molicel P28A and Sony Murata VCT5A models, the volume of the casing in voxels serves as a dependable metric for threshold calibration.

The algorithm sets an initial target cross-sectional area for the battery casing in a 2D slice. The thresholding process then iteratively adjusts the threshold value using a bisection method-style approach. In each iteration, the threshold is modified to measure the area of the segmented casing in the 2D slice, comparing it against the target area. This process continues, narrowing the range of possible threshold values, until the measured area closely matches the predetermined target area, within a specified tolerance.

This iterative method ensures thresholding is precisely adapted to the variations in imaging conditions and material appearances, characteristic of different experimental setups.

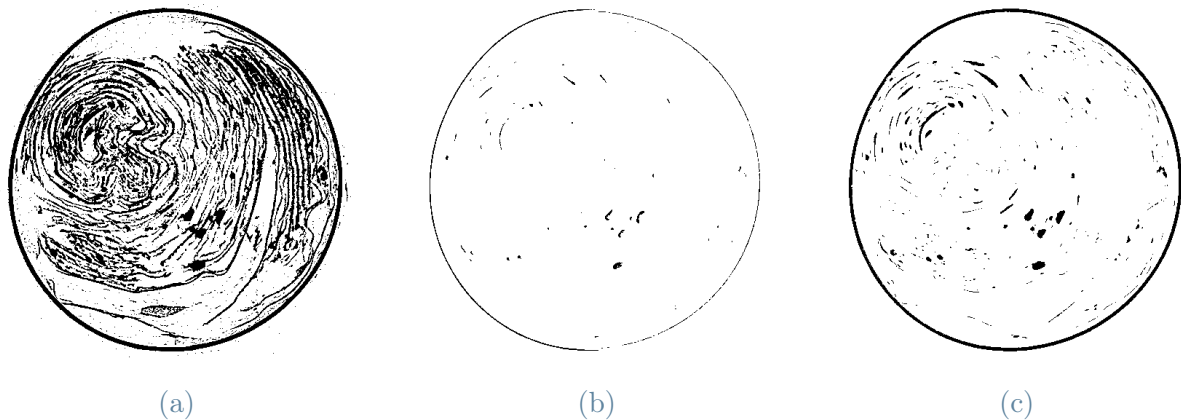


Figure 4.3: Threshold computation process for a P28A battery. **a** | Casing area is larger than target, threshold has to be increased. **b** | Casing area is smaller than target, threshold has to be decreased. **c** | Casing area is within tolerance of target, threshold is accepted.

4.1.2. 3D Segmentation

Segmentation of the reconstructed volumes is performed in 3D through a multi-step process. Initially, a binary mask is computed using the threshold value determined in Section 4.1.1, where voxels below the threshold are assigned a value of 0 (indicating background), and those above the threshold are assigned a value of 1 (indicating foreground). This mask is subsequently refined using morphological operations to eliminate smaller agglomerates and artifacts.

The `erosion` operation is employed to remove very small agglomerates and eliminate thin, straight-line reconstruction artifacts that frequently appear in the volumes. Following erosion, the `dilation` operation is applied to approximately restore the agglomerates to their original size. The number of iterations (`it`) for the erosion and dilation operations are set to 1 and 4, respectively, based on empirical observations. Finally, a logical AND operation is performed between the original mask and the refined mask to derive the final mask, ensuring only the agglomerates that were present in both the original and refined masks are retained.

$$\text{mask}[i] = \text{mask}[i] \wedge \text{dilation}(\text{erosion}(\text{mask}[i], \text{it}=1), \text{it}=4) \quad (4.1)$$

At this point the mask is still binary, with 0 representing the background and 1 representing the agglomerates and the casing. The next step is to label the agglomerates in the mask. This is done using the `label` function from the `scikit-image` library, which assigns a unique integer label to each connected component (i.e. a group of adjacent pixels sharing the same value) in the mask. Subsequently, the labels are reassigned based on the size of the connected components. This reassignment leverages the `regionprops` function from the `scikit-image` library to measure each component's size, allowing for the labels to be organized such that the casing is labeled 1, the largest agglomerate is labeled 2, the second largest 3, and so on.

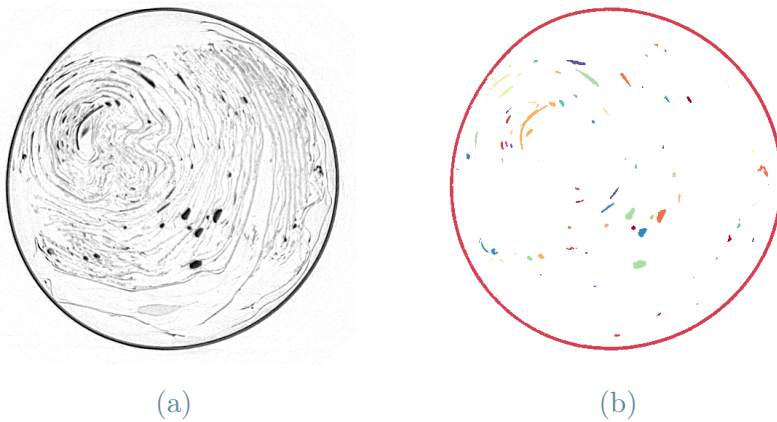


Figure 4.4: `ct` slice (a) and `mask` slice (b) of a P28A battery. Different colors indicate different labels.

The final label map `mask[i]` is then obtained by filtering the agglomerates smaller than a certain threshold. This threshold is set to 50 voxels, based on empirical observations. Agglomerates smaller than this threshold are considered noise and are removed from the label map.

4.1.3. Label propagation

The label propagation step is crucial for ensuring consistent labeling of the same agglomerate across different volumes, a key factor for accurate tracking throughout the thermal runaway process. The label propagation algorithm is implemented as follows:

1. **Increment current labels:** The labels of all identified objects in the current volume's mask `mask[i]` are incremented by adding the highest label number used in previous volume's mask `mask[i-1]` plus one. This step ensures that labels in the current mask do not overlap with labels from the previous mask, preserving the uniqueness of each label across volumes.
2. **Create label propagation map:** A mapping that identifies which labels from the current volume correspond to labels from the previous volume is constructed. This is done by analyzing regions where the current and previous masks overlap, using the areas of overlap to determine the most appropriate label correspondences (label with largest overlap gets propagated). This map is crucial for tracking the same agglomerates across different volumes.
3. **Generate lookup table:** A lookup table is initialized to facilitate the reassignment of labels in the current mask based on the label propagation map. This table is populated such that each entry corresponding to a current mask label points to the appropriate label from the previous volume, ensuring continuity in labeling.
4. **Handle new labels:** New labels in the current mask that do not have corresponding labels in the previous mask are identified (i.e., labels that represent agglomerates not present in the previous volume). These labels are assigned new, unique identifiers to maintain the distinction of each agglomerate.
5. **Apply lookup table:** The lookup table is applied to the current mask. This step reassigns labels in the current mask according to the established mappings, effectively propagating labels from the previous mask to the current one where applicable. This ensures that the same agglomerates are consistently labeled across sequential volumes.

Label propagation plays a critical role in the segmentation algorithm by ensuring that each agglomerate is tracked accurately across the dataset. This capability is essential for analyzing the evolution of copper agglomerates' speed and volume.

4.1.4. Filtering

Upon completing the segmentation and label propagation across all volumes, the algorithm progresses to the filtering phase, which is designed to refine the segmented label map by removing artifacts and ensuring that only meaningful agglomerates are retained for analysis. This phase encompasses several steps, each targeting specific types of artifacts or undesirable features within the segmentation results. The steps include:

1. **Region properties computation:** Initially, the algorithm computes the properties of all labeled regions across each volume using the `regionprops` function. This computation facilitates the identification and analysis of individual agglomerates based on their spatial characteristics.
2. **Transient agglomerates removal:** The algorithm identifies and marks for removal agglomerates that appear transient, i.e., those present in one volume but absent in both the preceding and succeeding volumes. This step is crucial for eliminating artifacts that do not correspond to persistent agglomerates, ensuring that only consistent features are analyzed further.
3. **Small agglomerates removal:** Agglomerates whose cumulative volume falls below a certain threshold are deemed insignificant and are also marked for removal. Notably, the size of each agglomerate is calculated in a four-dimensional manner, summing the voxel volume corresponding to a specific label across all segmented volumes. This operation filters out small artifacts and noise, focusing the analysis on agglomerates that appear in sequential volumes.
4. **Pre-thermal runaway agglomerates removal:** This step marks for removal the agglomerates appearing before the onset of thermal runaway, which are likely to be artifacts of the segmentation process rather than genuine features of interest. To systematically address this, the algorithm identifies and earmarks for removal all non-casing agglomerates that appear within the initial N volumes of the dataset, which represent the period before thermal runaway begins. The determination of N , the specific number of initial volumes to be considered, relies on a careful visual inspection of the dataset to ascertain the precise moment at which thermal runaway phenomena start to manifest.
5. **Label update and renaming:** Finally, the algorithm updates the label map by removing all labels marked for deletion in the previous steps and reassigning new labels to the remaining agglomerates.

4.2. Feature extraction

The segmentation algorithm yields a label map `mask` that accurately identifies copper agglomerates within the reconstructed volumes. This label map serves as the foundation for extracting a range of morphological and spatial features that are critical for analyzing the agglomerates' characteristics and behavior during thermal runaway. The features extracted from the label map for each agglomerate are reported in Table 4.1.

Feature	Description
<code>label</code>	Unique identifier for each agglomerate [int].
<code>t</code>	Time elapsed from the start of data acquisition [s]. Computed as i/fps , where i is the volume number and <code>fps</code> is the CT acquisition rate.
<code>x, y, z</code>	Centroid coordinates of the agglomerate, relative to the center of the battery [mm]. Computed by the <code>regionprops</code> function as the average of the voxel coordinates within each agglomerate and then multiplied by physical size of the voxel edge ($40 \mu\text{m}$).
<code>r</code>	Radial distance of the agglomerate's centroid from the central axis of the battery [mm]. Computed as Euclidean norm of (x, y) .
<code>r_section</code>	Position of the agglomerate's centroid within radial sections of the battery, categorized as <code>Core</code> , <code>Intermediate</code> , or <code>External</code> . <code>Core</code> is assigned if $0 < r < \frac{R}{3}$, <code>Intermediate</code> is assigned if $\frac{R}{3} < r < \frac{2R}{3}$, <code>External</code> otherwise, where R is the casing radius.
<code>z_section</code>	Vertical positioning of the agglomerate's centroid within the battery, categorized as <code>Top</code> , <code>Middle</code> , or <code>Bottom</code> . <code>Top</code> is assigned if $0 < z < \frac{Z}{3}$, <code>Middle</code> is assigned if $\frac{Z}{3} < z < \frac{2Z}{3}$, <code>Bottom</code> otherwise, where Z is the vertical FoV.
<code>vx, vy, vz</code>	Components of the agglomerate's velocity in the x , y , and z directions [mm/s]. Computed as $fps(e_i - e_{i-1})$ if the agglomerate is present in previous volume, with e equal to x , y or z . $(0, 0, 0)$ otherwise.
<code>v</code>	Magnitude of the agglomerate's velocity [mm/s]. Computed as Euclidean norm of (vx, vy, vz) .
<code>V</code>	Volume of the agglomerate [mm^3]. Computed by <code>regionprops</code> as the number of voxels within each agglomerate and then multiplied by physical voxel size ($(40 \mu\text{m})^3$).
<code>dVdt</code>	Rate of change of the agglomerate's volume over time [mm^3/s]. Computed as $fps(V_i - V_{i-1})$ if the agglomerate is present in previous volume, 0 otherwise.

Table 4.1: Agglomerates features extracted from the label map.

The above mentioned features are used to plot agglomerates total volume, average volume, total volume derivative, velocity and density as a function of time for each experiment. These plots are shown in Figure 4.5, and a short description is provided below.

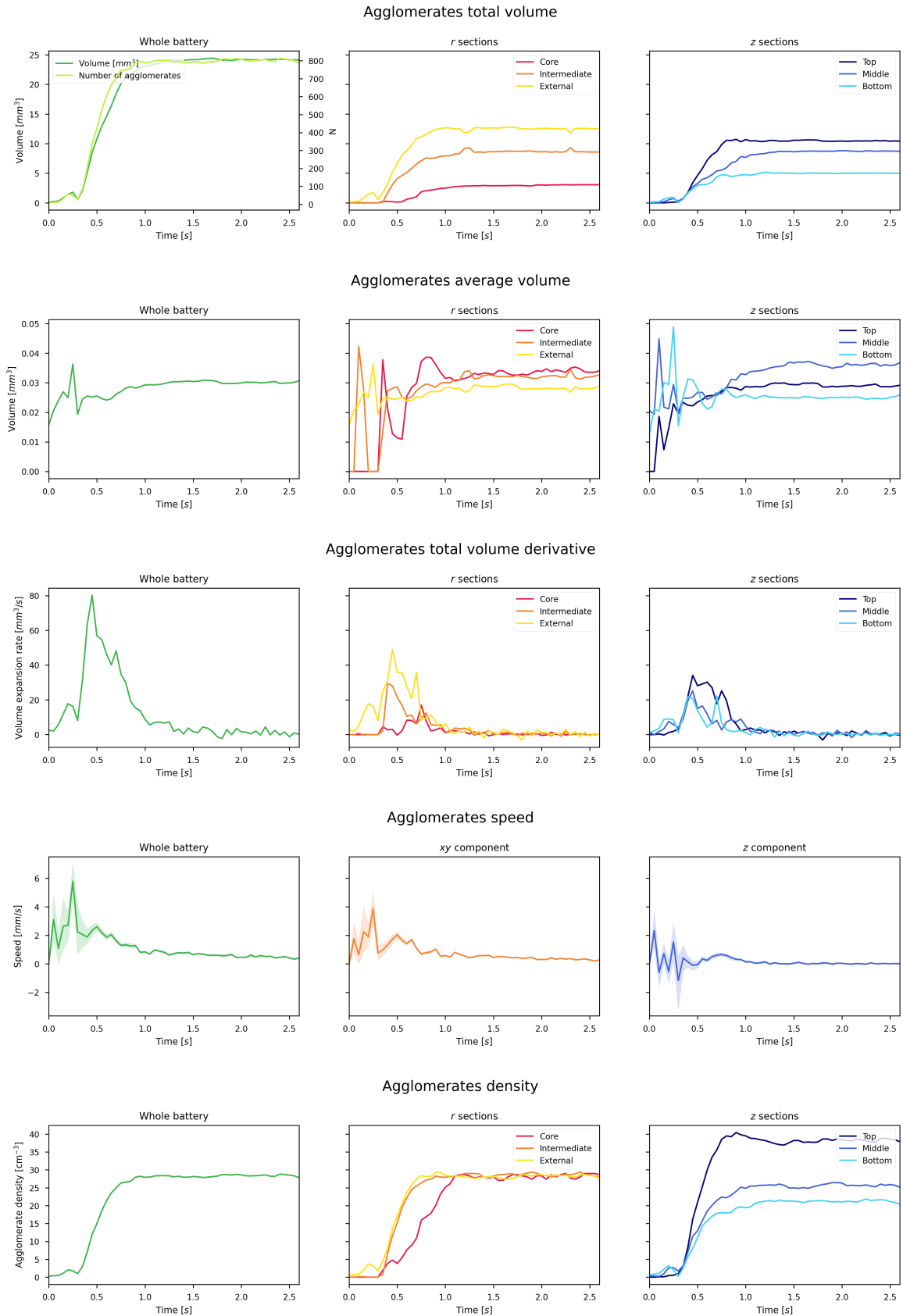


Figure 4.5: Agglomerates features plots for experiment P28A_Nail_Exp1.

- The **total volume** plot provides insights into the overall growth and evolution of agglomerates during thermal runaway. The total number of agglomerates is also indicated on the plot.
- The **average volume** plot complements the total volume plot, offering a more detailed view of the agglomerates' size distribution. This plot is particularly useful for comparing the size of agglomerates across different initiation methods and battery models.
- The **total volume derivative** plot highlights the speed at which agglomerates form and grow, providing valuable information on the progression of thermal runaway. This plot, combined with the agglomerate density plot, offers insights into uneven formation of agglomerates within different sections of the battery.
- The **velocity** plot offers insights into the spatial dynamics of agglomerates, revealing their movement and distribution within the battery.
- The **density** plot provides a measure of the spatial distribution of agglomerates within the battery, offering insights into their arrangement and concentration. Density is computed as the total number of agglomerates in each section (either radial or vertical) divided by the total volume of the section.

4.3. Visualization

Effective visualization of the segmentation results is crucial for both qualitative assessment and detailed analysis of the features identified within the tomography volumes. To this end, two main visualization approaches were employed, utilizing `napari` library [87] for 2D visualizations and Blender [88] for 3D representations.

4.3.1. 2D Visualization with Napari Viewer

The `napari` viewer was seamlessly integrated into the pipeline, offering an intuitive platform for visualizing 2D tomography slices and enabling the overlay of segmentation maps directly onto the corresponding slices (Figure 4.6). This capability is particularly useful for examining the segmentation accuracy and the spatial distribution of identified features within each slice. The viewer supports interactive exploration, with sliders allowing users to seamlessly navigate through different time points and slice levels. This interactive functionality enhances the ability to closely inspect the dynamic changes and progression of features, such as agglomerates, across the dataset.

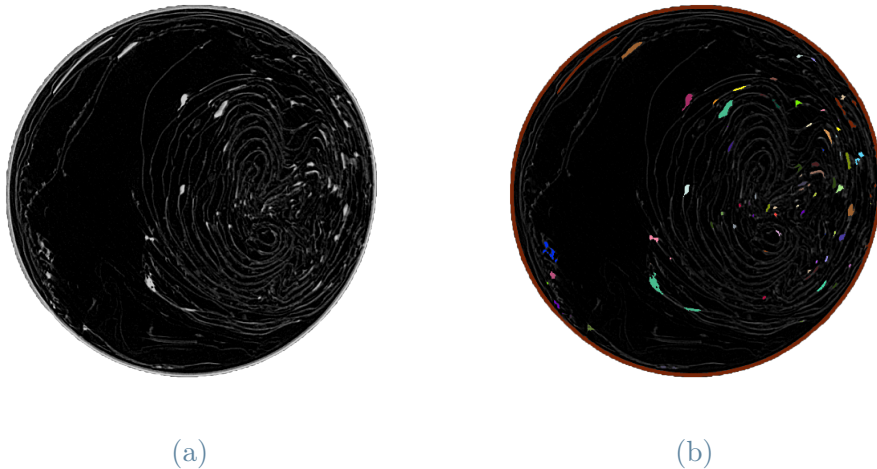


Figure 4.6: Napari viewer showing a `ct` slice (a) and an overlaid `mask` slice (b) of a P28A battery. Different colors indicate different labels. Inverted greyscale is used to better visualize the agglomerates.

4.3.2. 3D Visualization with Blender

For comprehensive 3D visualization, Blender was utilized to render volumetric representations of the segmented features. To facilitate this, a custom algorithm was developed to convert the segmentation maps into `STL` files, a format compatible with Blender. This conversion process enabled the detailed rendering of 3D volumes for each experiment, providing a comprehensive view of the agglomerates' morphology and spatial arrangement within the battery. Furthermore, to visualize the dynamic aspects of these features over time, a second algorithm was crafted to transform a sequence of `PNG` images (Blender output, Figure 4.7) into cohesive movies, offering a visual representation of the experimental outcomes. Examples can be found in the GitHub repository [86].

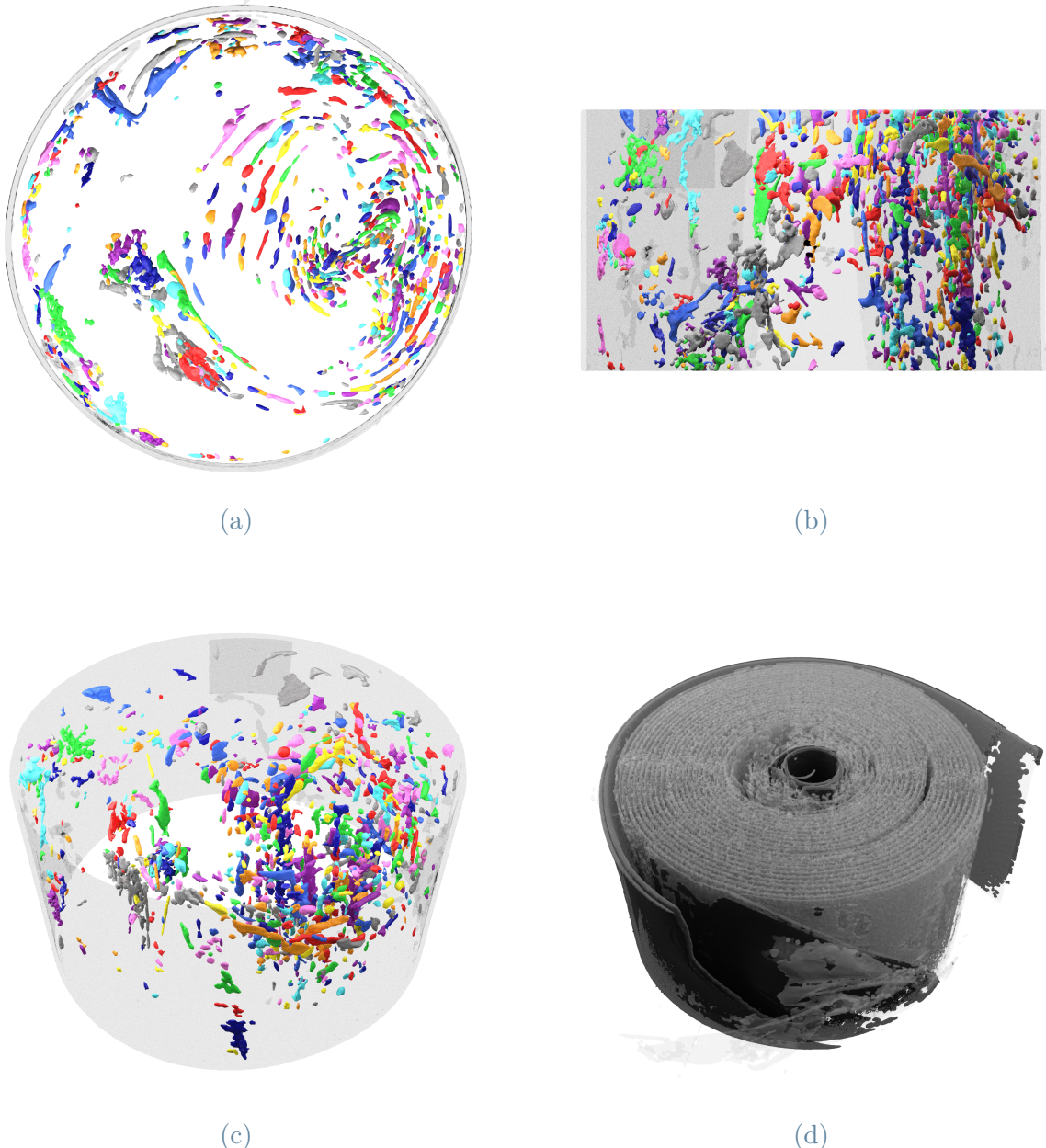


Figure 4.7: Top (a), side (b), and perspective (c) view renders of P28A battery agglomerates during thermal runaway showcase the agglomerates' spatial distribution and morphology. Orthographic renders for the top and side views enable detailed analysis of the agglomerates' radial and vertical density, respectively. A perspective render of the VCT5A battery's jellyroll post-sidewall rupture (d) offers insights into the internal structural changes.

5 | Results and Discussion

A total of 25 experiments were conducted during July 2022 beamtime, 5 for each of the following categories: P28A_Heat, P28A_Nail, VCT5A_Heat, VCT5A_Nail and P28B_ISC. Experiments involving P28A_Nail were excluded from the analysis as the batteries did not fail, attributed to a safety device present at the penetration site. Of the remaining 20 experiments, 9 resulted in extreme failure and sidewall rupture, where agglomerate formation was likely prevented by temperature drops post-breach. Additionally, two experiments were ignored due to corrupted reconstruction files, leaving 9 experiments eligible for agglomerate analysis.

Experiment name	Steady state total agglomerate volume [mm ³]	Steady state average agglomerate volume [mm ³]	Steady state agglomerate density [cm ⁻³]
P28A_Heat_Exp1	24.1	0.0307 ± 0.0676	27.8
P28A_Heat_Exp2	48.3	0.0246 ± 0.0394	69.4
P28A_Heat_Exp3_3	32.4	0.0221 ± 0.0349	51.8
P28A_Heat_Exp4_2	43.9	0.0228 ± 0.0364	68.1
P28A_Heat_Exp5_3	35.8	0.0272 ± 0.111	46.6
VCT5A_Nail_Exp4	54.5	0.0322 ± 0.0631	59.9
VCT5A_Nail_Exp5	49.0	0.0400 ± 0.0651	43.3
VCT5A_Heat_Exp2	50.6	0.0495 ± 0.0988	36.2
VCT5A_Heat_Exp5	68.8	0.0652 ± 0.149	37.4

Table 5.1: Agglomerates feature comparison across different experiments.

5.1. Initiation Method Comparison

While significant conclusions cannot be drawn from the data in Table 5.1, valuable insights emerge from examining the agglomerate features plots and the renderings. Notably, for the **heat** initiation method, agglomerates are observed to form initially in the outermost part of the battery, moving gradually towards the center. This pattern likely results from

the heat gun's focus on the casing, creating a temperature gradient where the temperature is lower in the center. This gradient facilitates the melting of metals close to the battery casing, with a gradual progression towards the center as the heat diffuses inward. This phenomenon, illustrated in Figures 5.1 and 5.2, is apparent in both P28A and VCT5A batteries, despite it being less distinct in the latter.

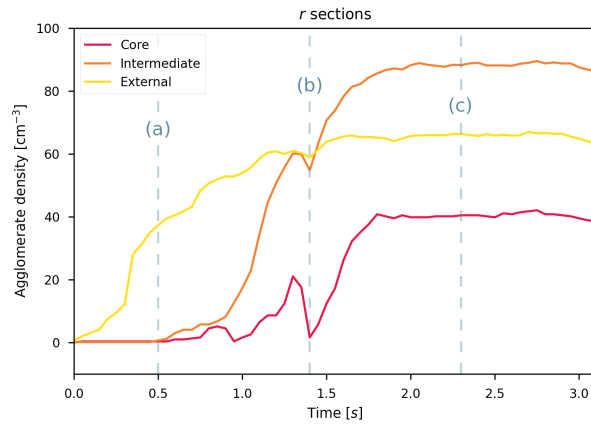


Figure 5.1: P28A_Heat_Exp4_2: Plot of the agglomerate density as a function of time for the three radial sections of the battery. Agglomerate density increases first in the outermost section (a), followed by the middle section (b) and the innermost section (c). Renderings related to (a), (b) and (c) are shown in Figure 5.2a, 5.2b and 5.2c, respectively.

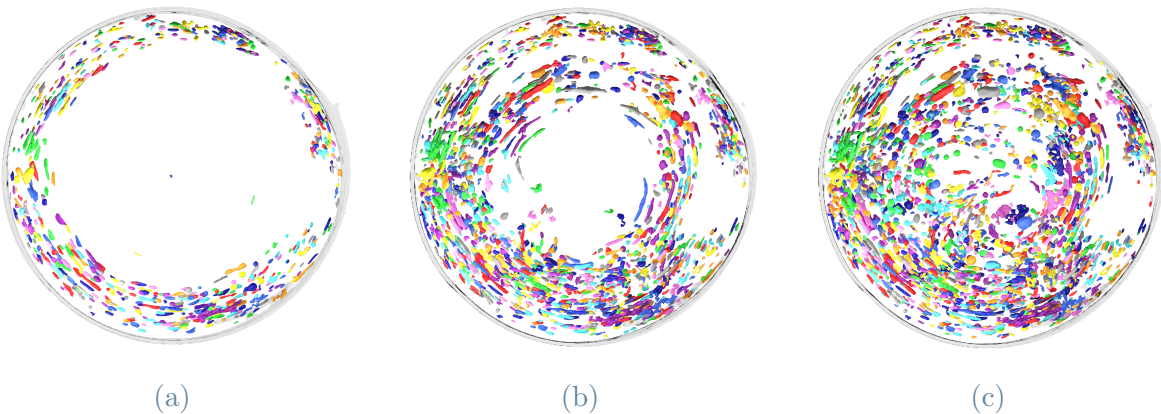


Figure 5.2: P28A_Heat_Exp4_2: Agglomerate renderings (top view) after 0.5 (a), 1.4 (b) and 2.3 s (c) from the start of the thermal runaway. The agglomerates initially form in the outermost section of the battery, moving gradually towards the center. This pattern is consistent with the agglomerate density plot shown in Figure 5.1.

In contrast, the **nail** initiation method exhibits an opposite trend, illustrated in Figures 5.3 and 5.4, with agglomerates forming centrally and spreading towards the casing, attributed

to the nail's penetration along the battery's axis.

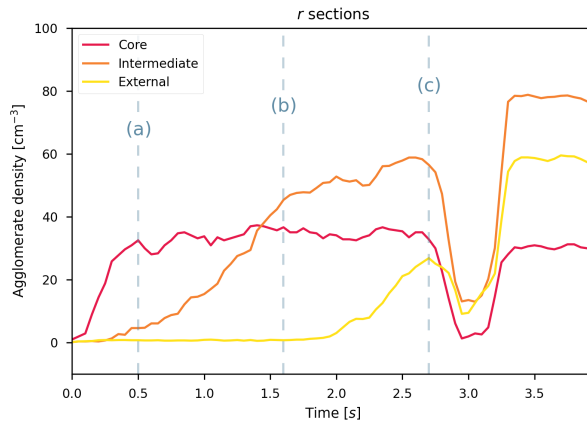


Figure 5.3: VCT5A_Nail_Exp4: Plot of the agglomerate density as a function of time for the three radial sections of the battery. Agglomerate density increases first in the innermost section (a), followed by the middle section (b) and finally the outermost section (c). Renderings related to (a), (b) and (c) are shown in Figure 5.4a, 5.4b and 5.4c, respectively.



Figure 5.4: VCT5A_Nail_Exp4: Agglomerate renderings after 0.5 (a), 1.6 (b) and 2.7 s (c) from the start of the thermal runaway. The agglomerates are initially formed in the innermost section of the battery, moving gradually towards the casing. This pattern is consistent with the agglomerate density plot shown in Figure 5.3.

The trough in the agglomerate density plot between 2.9 and 3.2 s in Figure 5.3 is attributed to the activation of the venting system. By expelling gaseous and non-gaseous products from the top of the battery, the venting system aims to release the pressure built up inside the battery, preventing sidewall rupture. This hypothesis is supported by the related side view renderings, which show agglomerates moving towards the top of the battery.

Generally, nail experiments exhibited a longer thermal runaway duration before reaching steady state, likely due to the lower overall battery temperature before thermal runaway with respect to heat experiments. The time required to reach steady state was observed to be between 1 and 2 s for heat experiments, while in nail experiments it was between 3.5 and 4 s.

ISC experiments displayed markedly violent battery failure (Figure 5.5), likely due to the rapid heat release characteristic of the internal short circuit initiation method. Sidewall rupture occurred in each of the experiments, facilitating the heat release into the surrounding environment, thus preventing the battery's interior from reaching the temperatures necessary for metal melting.

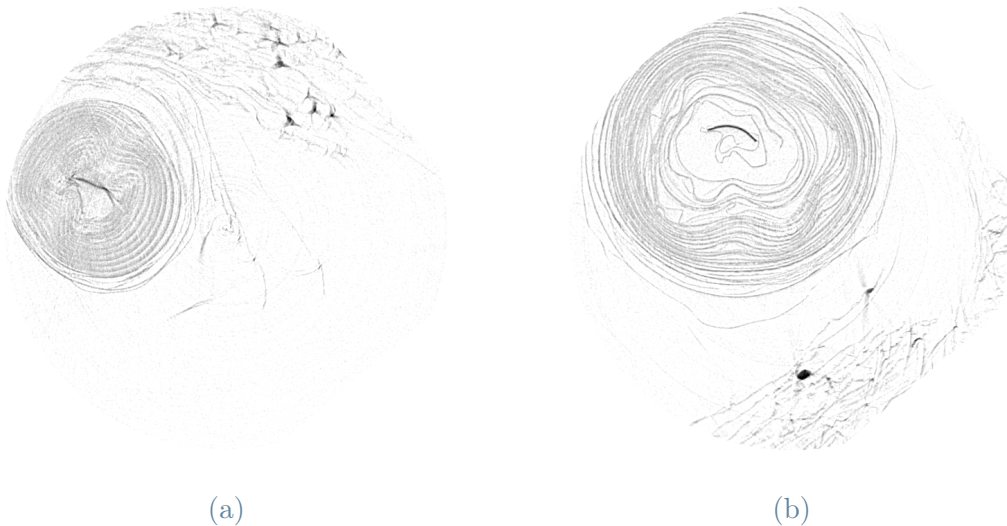


Figure 5.5: Slices of P28B batteries after thermal runaway in experiments P28B_ISC_Exp3 (a) and P28B_ISC_Exp5 (b). The batteries failed violently, with the sidewall rupturing and the interior of the battery being exposed to the environment.

5.2. P28A - VCT5A Comparison

Given that the P28A_Nail experiments are excluded from the analysis, the comparison between P28A and VCT5A batteries will be based solely on the experiments detailed in Table 5.1.

The boxplots in Figure 5.6 show the total agglomerate volume, average agglomerate volume and agglomerate density for each battery type. VCT5A batteries exhibit a higher total agglomerate volume and average agglomerate volume, while P28A batteries show a slightly higher agglomerate density.

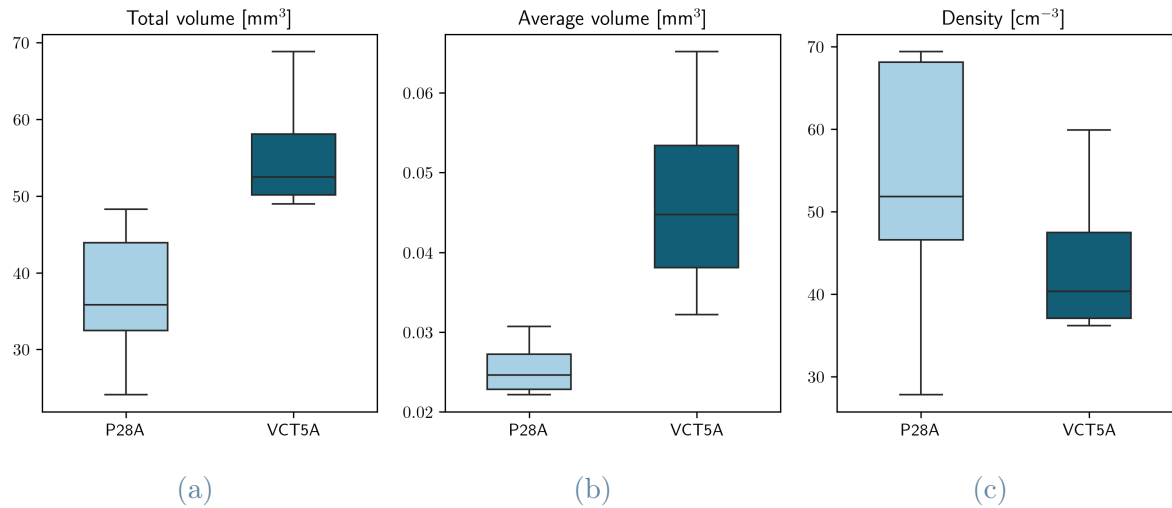


Figure 5.6: Boxplots for the features shown in Table 5.1, comparing P28A and VCT5A battery types. Total agglomerate volume is shown in (a), average agglomerate volume in (b) and agglomerate density in (c). Plot (b) is built on the average agglomerate volume for each experiment, rather than the volume of each agglomerate (see Figure 5.7b).

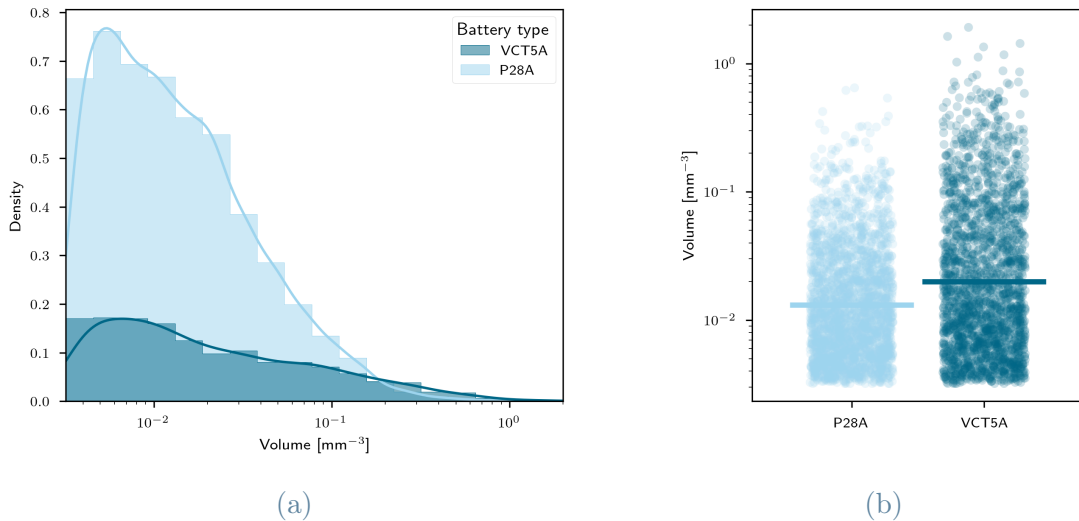


Figure 5.7: Agglomerate size plots in logarithmic scale for P28A and VCT5A battery types. Histogram and kernel density estimation plots are shown in (a), while the point plot is shown in (b). The point plot also shows the average agglomerate volume for each battery type. A longer tail is observed for VCT5A battery.

It's noted that boxplot 5.6b uses the average agglomerate volume per experiment for comparison, which may not fully capture the variability seen when considering each agglomerate's volume individually. This variability is illustrated in the agglomerate size

plots in Figure 5.7, where a longer tail is observed for VCT5A batteries, indicating a higher number of large agglomerates (this result is consistent with the renderings shown in Figure 5.8).



Figure 5.8: Steady state renderings for P28A and VCT5A batteries. The rendering for P28A_Heat_Exp4_2 is shown in (a), while the rendering for VCT5A_Heat_Exp5 is shown in (b). The VCT5A rendering clearly shows a higher number of large agglomerates.

To statistically validate the observed differences in agglomerate volume distribution between the two battery types, the application of the ANOVA and Welch statistical tests is proposed, aiming to demonstrate a significant difference in the mean values of the two distributions.

One-way ANOVA was initially applied, yielding an F-statistic of approximately $2.72 \cdot 10^2$ and a highly significant p-value ($3.60 \cdot 10^{-60}$), suggesting significant differences between the groups. However, given the underlying assumptions of normality and homogeneity of variances (homoscedasticity) associated with ANOVA, which our data violated, a more robust test was employed. Welch's t-test, better suited for datasets that do not meet these assumptions [89], was then conducted. It produced a t-statistic of $-1.14 \cdot 10^1$ and a highly significant p-value ($4.09 \cdot 10^{-29}$), conclusively indicating a significant difference in mean agglomerate volumes between P28A and VCT5A batteries, reinforcing the initial ANOVA findings under more relaxed assumptions regarding data distribution and variance.

6 | Conclusions and Future Developments

The development of a fast tomography method at the European Synchrotron Radiation Facility (ESRF) for observing lithium-ion batteries during thermal runaway has marked a significant advancement in battery research. This innovative approach has not only shed light on the complex dynamics of thermal runaway but has also provided valuable three-dimensional data that were previously unattainable. The establishment of a comprehensive pipeline for data analysis has revealed the potential to extract detailed information about agglomerate formation within batteries, offering insights critical for understanding battery failure mechanisms.

This thesis contributes a foundational framework for future research in agglomerate analysis and simulation, with the data serving as a potent validation tool for thermal runaway simulations. Looking ahead, there is a compelling opportunity to refine the segmentation process to enhance accuracy further. Such improvements could enable more precise measurements of agglomerate formation speed and provide indirect estimations of battery heat flow, a key parameter in battery safety and performance.

Moreover, investigating the chemical composition of the agglomerates through Energy-dispersive X-ray spectroscopy (EDX) presents a promising avenue for future work. This analysis could offer deeper insights into the material transformations that occur during battery failure, enriching our understanding of the processes at play.

Ultimately, the insights gleaned from this work hold the potential to significantly impact the design of safer, more reliable lithium-ion batteries. By advancing our understanding of thermal runaway and improving our ability to predict and mitigate its effects, this research paves the way toward enhancing battery safety protocols and design standards, contributing to the broader goal of sustainable and safe energy storage solutions.

Bibliography

- [1] Susan Solomon et al. “Irreversible Climate Change Due to Carbon Dioxide Emissions”. In: *Proceedings of the National Academy of Sciences* 106.6 (Feb. 2009), pp. 1704–1709. DOI: [10.1073/pnas.0812721106](https://doi.org/10.1073/pnas.0812721106).
- [2] *Trends in Atmospheric Carbon Dioxide*. Tech. rep. NOAA/GML, 2023.
- [3] World Health Organization. *Ambient Air Pollution: A Global Assessment of Exposure and Burden of Disease*. Geneva: World Health Organization, 2016. ISBN: 978-92-4-151135-3.
- [4] *Greenhouse Gas Emissions from Energy Data Explorer*. Tech. rep. International Energy Agency (IEA), 2023.
- [5] Ghassan Zubi et al. “The Lithium-Ion Battery: State of the Art and Future Perspectives”. In: *Renewable and Sustainable Energy Reviews* 89 (June 2018), pp. 292–308. ISSN: 1364-0321. DOI: [10.1016/j.rser.2018.03.002](https://doi.org/10.1016/j.rser.2018.03.002).
- [6] Daniele Stampatori, Pier Paolo Raimondi, and Michel Noussan. “Li-Ion Batteries: A Review of a Key Technology for Transport Decarbonization”. In: *Energies* 13.10 (Jan. 2020), p. 2638. ISSN: 1996-1073. DOI: [10.3390/en13102638](https://doi.org/10.3390/en13102638).
- [7] Reiner Korthauer, ed. *Lithium-Ion Batteries: Basics and Applications*. Trans. by Michael Wuest. Berlin [Heidelberg]: Springer, 2018. ISBN: 978-3-662-53069-6. DOI: [10.1007/978-3-662-53071-9](https://doi.org/10.1007/978-3-662-53071-9).
- [8] Shuai Ma et al. “Temperature Effect and Thermal Impact in Lithium-Ion Batteries: A Review”. In: *Progress in Natural Science: Materials International* 28.6 (Dec. 2018), pp. 653–666. ISSN: 1002-0071. DOI: [10.1016/j.pnsc.2018.11.002](https://doi.org/10.1016/j.pnsc.2018.11.002).
- [9] Gang Ning, Bala Haran, and Branko N. Popov. “Capacity Fade Study of Lithium-Ion Batteries Cycled at High Discharge Rates”. In: *Journal of Power Sources* 117.1 (May 2003), pp. 160–169. ISSN: 0378-7753. DOI: [10.1016/S0378-7753\(03\)00029-6](https://doi.org/10.1016/S0378-7753(03)00029-6).

- [10] M. R. Palacín and A. de Guibert. “Why Do Batteries Fail?” In: *Science* 351.6273 (Feb. 2016), p. 1253292. DOI: [10.1126/science.1253292](https://doi.org/10.1126/science.1253292).
- [11] Daniel H. Doughty and E. Peter Roth. “A General Discussion of Li Ion Battery Safety”. In: *The Electrochemical Society Interface* 21.2 (Jan. 2012), p. 37. ISSN: 1944-8783. DOI: [10.1149/2.F03122if](https://doi.org/10.1149/2.F03122if).
- [12] John B. Goodenough and Kyu-Sung Park. “The Li-Ion Rechargeable Battery: A Perspective”. In: *Journal of the American Chemical Society* 135.4 (Jan. 2013), pp. 1167–1176. ISSN: 0002-7863. DOI: [10.1021/ja3091438](https://doi.org/10.1021/ja3091438).
- [13] Arumugam Manthiram. “A Reflection on Lithium-Ion Battery Cathode Chemistry”. In: *Nature Communications* 11.1 (Mar. 2020), p. 1550. ISSN: 2041-1723. DOI: [10.1038/s41467-020-15355-0](https://doi.org/10.1038/s41467-020-15355-0).
- [14] Yemeserach Mekonnen, Aditya Sundararajan, and Arif I. Sarwat. “A Review of Cathode and Anode Materials for Lithium-Ion Batteries”. In: *SoutheastCon 2016*. Mar. 2016, pp. 1–6. DOI: [10.1109/SECON.2016.7506639](https://doi.org/10.1109/SECON.2016.7506639).
- [15] P. U. Nzereogu et al. “Anode Materials for Lithium-Ion Batteries: A Review”. In: *Applied Surface Science Advances* 9 (June 2022), p. 100233. ISSN: 2666-5239. DOI: [10.1016/j.apsadv.2022.100233](https://doi.org/10.1016/j.apsadv.2022.100233).
- [16] Kang Xu. “Nonaqueous Liquid Electrolytes for Lithium-Based Rechargeable Batteries”. In: *Chemical Reviews* 104.10 (Oct. 2004), pp. 4303–4418. ISSN: 0009-2665. DOI: [10.1021/cr030203g](https://doi.org/10.1021/cr030203g).
- [17] Doron Aurbach et al. “The Study of Electrolyte Solutions Based on Ethylene and Diethyl Carbonates for Rechargeable Li Batteries: II . Graphite Electrodes”. In: *Journal of The Electrochemical Society* 142.9 (Sept. 1995), p. 2882. ISSN: 1945-7111. DOI: [10.1149/1.2048659](https://doi.org/10.1149/1.2048659).
- [18] J. Y. Song, Y. Y. Wang, and C. C. Wan. “Review of Gel-Type Polymer Electrolytes for Lithium-Ion Batteries”. In: *Journal of Power Sources* 77.2 (Feb. 1999), pp. 183–197. ISSN: 0378-7753. DOI: [10.1016/S0378-7753\(98\)00193-1](https://doi.org/10.1016/S0378-7753(98)00193-1).
- [19] Evan Walter Clark Spotte-Smith et al. “Toward a Mechanistic Model of Solid-Electrolyte Interphase Formation and Evolution in Lithium-Ion Batteries”. In: *ACS Energy Letters* 7.4 (Apr. 2022), pp. 1446–1453. DOI: [10.1021/acsenergylett.2c00517](https://doi.org/10.1021/acsenergylett.2c00517).

- [20] Pankaj Arora and Zhengming (John) Zhang. “Battery Separators”. In: *Chemical Reviews* 104.10 (Oct. 2004), pp. 4419–4462. ISSN: 0009-2665. DOI: 10.1021/cr020738u.
- [21] Richard S. Bladwin. *A Review of State-of-the-Art Separator Materials for Advanced Lithium-Based Batteries for Future Aerospace Missions*. Tech. rep. E-16879. Mar. 2009.
- [22] Pengcheng Zhu et al. “A Review of Current Collectors for Lithium-Ion Batteries”. In: *Journal of Power Sources* 485 (Feb. 2021), p. 229321. ISSN: 0378-7753. DOI: 10.1016/j.jpowsour.2020.229321.
- [23] “List of Battery Sizes”. In: *Wikipedia* (Feb. 2024).
- [24] Sabri Baazouzi et al. “Design, Properties, and Manufacturing of Cylindrical Li-Ion Battery Cells—A Generic Overview”. In: *Batteries* 9.6 (June 2023), p. 309. ISSN: 2313-0105. DOI: 10.3390/batteries9060309.
- [25] Abhishek Das et al. “Joining Technologies for Automotive Battery Systems Manufacturing”. In: *World Electric Vehicle Journal* 9.2 (Aug. 2018), p. 22. ISSN: 2032-6653. DOI: 10.3390/wevj9020022.
- [26] Shriram Santhanagopalan, Chuanbo Yang, and Ahmad Pesaran. *Modeling Lithium Ion Battery Safety: Venting of Pouch Cells; NREL (National Renewable Energy Laboratory)*. Tech. rep. NREL/MP-5400-60043. National Renewable Energy Lab. (NREL), Golden, CO (United States), July 2013. DOI: 10.2172/1214951.
- [27] Yuqiong Kang et al. “Binder-Free Electrodes and Their Application for Li-Ion Batteries”. In: *Nanoscale Research Letters* 15.1 (May 2020), p. 112. ISSN: 1556-276X. DOI: 10.1186/s11671-020-03325-w.
- [28] Qingsong Wang et al. “A Review of Lithium Ion Battery Failure Mechanisms and Fire Prevention Strategies”. In: *Progress in Energy and Combustion Science* 73 (July 2019), pp. 95–131. ISSN: 0360-1285. DOI: 10.1016/j.pecs.2019.03.002.
- [29] Corey T. Love et al. “Innovating Safe Lithium-Ion Batteries Through Basic to Applied Research”. In: *Journal of Electrochemical Energy Conversion and Storage* 15.011006 (Oct. 2017). ISSN: 2381-6872. DOI: 10.1115/1.4038075.
- [30] Florian Schipper et al. “Review—Recent Advances and Remaining Challenges for Lithium Ion Battery Cathodes”. In: *Journal of The Electrochemical Society* 164.1 (Dec. 2016), A6220. ISSN: 1945-7111. DOI: 10.1149/2.0351701jes.

- [31] Xuning Feng et al. "Thermal Runaway Mechanism of Lithium Ion Battery for Electric Vehicles: A Review". In: *Energy Storage Materials* 10 (Jan. 2018), pp. 246–267. ISSN: 2405-8297. DOI: 10.1016/j.ensm.2017.05.013.
- [32] Yuqing Chen et al. "A Review of Lithium-Ion Battery Safety Concerns: The Issues, Strategies, and Testing Standards". In: *Journal of Energy Chemistry* 59 (Aug. 2021), pp. 83–99. ISSN: 2095-4956. DOI: 10.1016/j.jecchem.2020.10.017.
- [33] P. G. Balakrishnan, R. Ramesh, and T. Prem Kumar. "Safety Mechanisms in Lithium-Ion Batteries". In: *Journal of Power Sources* 155.2 (Apr. 2006), pp. 401–414. ISSN: 0378-7753. DOI: 10.1016/j.jpowsour.2005.12.002.
- [34] Qingsong Wang et al. "Thermal Runaway Caused Fire and Explosion of Lithium Ion Battery". In: *Journal of Power Sources* 208 (June 2012), pp. 210–224. ISSN: 0378-7753. DOI: 10.1016/j.jpowsour.2012.02.038.
- [35] Hossein Maleki et al. "Thermal Stability Studies of Li-Ion Cells and Components". In: *Journal of The Electrochemical Society* 146.9 (Sept. 1999), p. 3224. ISSN: 1945-7111. DOI: 10.1149/1.1392458.
- [36] Donal P. Finegan et al. "Investigating Lithium-Ion Battery Materials during Overcharge-Induced Thermal Runaway: An Operando and Multi-Scale X-ray CT Study". In: *Physical Chemistry Chemical Physics* 18.45 (2016), pp. 30912–30919. DOI: 10.1039/C6CP04251A.
- [37] Guifang Guo et al. "Three-Dimensional Thermal Finite Element Modeling of Lithium-Ion Battery in Thermal Abuse Application". In: *Journal of Power Sources* 195.8 (Apr. 2010), pp. 2393–2398. ISSN: 0378-7753. DOI: 10.1016/j.jpowsour.2009.10.090.
- [38] Gi-Heon Kim, Ahmad Pesaran, and Robert Spotnitz. "A Three-Dimensional Thermal Abuse Model for Lithium-Ion Cells". In: *Journal of Power Sources* 170.2 (July 2007), pp. 476–489. ISSN: 0378-7753. DOI: 10.1016/j.jpowsour.2007.04.018.
- [39] Joshua Lamb and Christopher J. Orendorff. "Evaluation of Mechanical Abuse Techniques in Lithium Ion Batteries". In: *Journal of Power Sources* 247 (Feb. 2014), pp. 189–196. ISSN: 0378-7753. DOI: 10.1016/j.jpowsour.2013.08.066.
- [40] Roland Jung et al. "Oxygen Release and Its Effect on the Cycling Stability of LiNixMnyCozO₂ (NMC) Cathode Materials for Li-Ion Batteries". In: *Journal of The Electrochemical Society* 164.7 (May 2017), A1361. ISSN: 1945-7111. DOI: 10.1149/2.0021707jes.

- [41] Jing Wang et al. "Alumina/Phenolphthalein Polyetherketone Ceramic Composite Polypropylene Separator Film for Lithium Ion Power Batteries". In: *Electrochimica Acta* 159 (Mar. 2015), pp. 61–65. ISSN: 0013-4686. DOI: 10.1016/j.electacta.2015.01.208.
- [42] Dongsheng Ren et al. "An Electrochemical-Thermal Coupled Overcharge-to-Thermal Runaway Model for Lithium Ion Battery". In: *Journal of Power Sources* 364 (Oct. 2017), pp. 328–340. ISSN: 0378-7753. DOI: 10.1016/j.jpowsour.2017.08.035.
- [43] J.-M. Tarascon and M. Armand. "Issues and Challenges Facing Rechargeable Lithium Batteries". In: *Nature* 414.6861 (Nov. 2001), pp. 359–367. ISSN: 1476-4687. DOI: 10.1038/35104644.
- [44] Se-Hee Kim et al. "A Shape-Deformable and Thermally Stable Solid-State Electrolyte Based on a Plastic Crystal Composite Polymer Electrolyte for Flexible/Safer Lithium-Ion Batteries". In: *Journal of Materials Chemistry A* 2.28 (2014), pp. 10854–10861. DOI: 10.1039/C4TA00494A.
- [45] Binghe Liu et al. "Safety Issues and Mechanisms of Lithium-Ion Battery Cell upon Mechanical Abusive Loading: A Review". In: *Energy Storage Materials* 24 (Jan. 2020), pp. 85–112. ISSN: 2405-8297. DOI: 10.1016/j.ensm.2019.06.036.
- [46] *Some Problems of Chemical Kinetics and Reactivity*. Elsevier, 1958. ISBN: 978-1-4831-6747-3. DOI: 10.1016/C2013-0-06654-6.
- [47] Xuan Liu et al. "Comprehensive Calorimetry of the Thermally-Induced Failure of a Lithium Ion Battery". In: *Journal of Power Sources* 280 (Apr. 2015), pp. 516–525. ISSN: 0378-7753. DOI: 10.1016/j.jpowsour.2015.01.125.
- [48] Xuning Feng et al. "Thermal Runaway Features of Large Format Prismatic Lithium Ion Battery Using Extended Volume Accelerating Rate Calorimetry". In: *Journal of Power Sources* 255 (June 2014), pp. 294–301. ISSN: 0378-7753. DOI: 10.1016/j.jpowsour.2014.01.005.
- [49] National Standard of the People's Republic of China. *GB/T 31485-2015*. May 2015.
- [50] Society of Automotive Engineers (SAE). *J2464-202108*. Aug. 2021.
- [51] International Electrotechnical Commission (IEC). *IEC 62133-2:2017*. July 2021.
- [52] United Nations. *UN38.3*. Jan. 2015.
- [53] Japanese Industrial Standard (JIS). *JIS C 8714*. Oct. 2017.

- [54] Underwriters Laboratories (UL). *UL 2580*. June 2022.
- [55] International Standardization Organization (ISO). *ISO16750-2:2023*. July 2023.
- [56] Takahisa Ohsaki et al. “Overcharge Reaction of Lithium-Ion Batteries”. In: *Journal of Power Sources*. Selected Papers Presented at the 12th International Meeting on Lithium Batteries 146.1 (Aug. 2005), pp. 97–100. ISSN: 0378-7753. DOI: 10.1016/j.jpowsour.2005.03.105.
- [57] J. Arai et al. “In Situ Solid State ^{7}Li NMR Observations of Lithium Metal Deposition during Overcharge in Lithium Ion Batteries”. In: *Journal of The Electrochemical Society* 162.6 (Mar. 2015), A952. ISSN: 1945-7111. DOI: 10.1149/2.0411506jes.
- [58] Diego Lisbona and Timothy Snee. “A Review of Hazards Associated with Primary Lithium and Lithium-Ion Batteries”. In: *Process Safety and Environmental Protection*. Special Issue: Centenary of the Health and Safety Issue 89.6 (Nov. 2011), pp. 434–442. ISSN: 0957-5820. DOI: 10.1016/j.psep.2011.06.022.
- [59] Hui-Fang Li, Jun-Kui Gao, and Shao-Li Zhang. “Effect of Overdischarge on Swelling and Recharge Performance of Lithium Ion Cells”. In: *Chinese Journal of Chemistry* 26.9 (2008), pp. 1585–1588. ISSN: 1614-7065. DOI: 10.1002/cjoc.200890286.
- [60] Dongxu Ouyang et al. “Investigation of a Commercial Lithium-Ion Battery under Overcharge/over-Discharge Failure Conditions”. In: *RSC Advances* 8.58 (2018), pp. 33414–33424. DOI: 10.1039/C8RA05564E.
- [61] Matilda Fransson. “Understanding Battery Failure Using High-Speed X-ray Imaging”. PhD thesis. University College London, 2024.
- [62] Zhi Wang et al. “Thermal Runaway and Fire Behaviors of Large-Scale Lithium Ion Batteries with Different Heating Methods”. In: *Journal of Hazardous Materials* 379 (Nov. 2019), p. 120730. ISSN: 0304-3894. DOI: 10.1016/j.jhazmat.2019.06.007.
- [63] Todd M. Bandhauer, Srinivas Garimella, and Thomas F. Fuller. “A Critical Review of Thermal Issues in Lithium-Ion Batteries”. In: *Journal of The Electrochemical Society* 158.3 (Jan. 2011), R1. ISSN: 1945-7111. DOI: 10.1149/1.3515880.
- [64] EUCAR. *Battery Requirements for Future Automotive Applications*. July 2019.
- [65] Muthukrishnan Kaliaperumal et al. “Cause and Mitigation of Lithium-Ion Battery Failure—A Review”. In: *Materials* 14.19 (Sept. 2021), p. 5676. ISSN: 1996-1944. DOI: 10.3390/ma14195676.

- [66] Donal P. Finegan et al. “Identifying the Cause of Rupture of Li-Ion Batteries during Thermal Runaway”. In: *Advanced Science* 5.1 (2018), p. 1700369. ISSN: 2198-3844. DOI: 10.1002/advs.201700369.
- [67] Patrick Pietsch et al. “Combining Operando Synchrotron X-ray Tomographic Microscopy and Scanning X-ray Diffraction to Study Lithium Ion Batteries”. In: *Scientific Reports* 6.1 (June 2016), p. 27994. ISSN: 2045-2322. DOI: 10.1038/srep27994.
- [68] Martin T. M. Pham et al. “Correlative Acoustic Time-of-Flight Spectroscopy and X-ray Imaging to Investigate Gas-Induced Delamination in Lithium-Ion Pouch Cells during Thermal Runaway”. In: *Journal of Power Sources* 470 (Sept. 2020), p. 228039. ISSN: 0378-7753. DOI: 10.1016/j.jpowsour.2020.228039.
- [69] Donal P. Finegan et al. “In-Operando High-Speed Tomography of Lithium-Ion Batteries during Thermal Runaway”. In: *Nature Communications* 6.1 (Apr. 2015), p. 6924. ISSN: 2041-1723. DOI: 10.1038/ncomms7924.
- [70] Stuart R. Stock. *MicroComputed Tomography: Methodology and Applications*. 1st ed. CRC Press, Oct. 2018. ISBN: 978-1-315-21918-9. DOI: 10.1201/9781420058772.
- [71] ESRF Accelerators. <https://www.esrf.fr/home/UsersAndScience/Accelerators.html>.
- [72] ESRF - ID19. <https://www.esrf.fr/home/UsersAndScience/Experiments/StructMaterials/ID19.html>.
- [73] BLISS Documentation. <https://bliss.gitlab-pages.esrf.fr/bliss/master/>.
- [74] Philip J. Withers et al. “X-Ray Computed Tomography”. In: *Nature Reviews Methods Primers* 1.1 (Feb. 2021), pp. 1–21. ISSN: 2662-8449. DOI: 10.1038/s43586-021-00015-4.
- [75] Marco Endrizzi. “X-Ray Phase-Contrast Imaging”. In: *Nuclear Instruments and Methods in Physics Research Section A: Accelerators, Spectrometers, Detectors and Associated Equipment*. Radiation Imaging Techniques and Applications 878 (Jan. 2018), pp. 88–98. ISSN: 0168-9002. DOI: 10.1016/j.nima.2017.07.036.
- [76] Karin Hellerhoff et al. “Assessment of Intraductal Carcinoma in Situ (DCIS) Using Grating-Based X-ray Phase-Contrast CT at Conventional X-ray Sources: An Experimental Ex-Vivo Study”. In: *PLOS ONE* 14.1 (Jan. 2019), e0210291. ISSN: 1932-6203. DOI: 10.1371/journal.pone.0210291.

- [77] D. Paganin et al. “Simultaneous Phase and Amplitude Extraction from a Single Defocused Image of a Homogeneous Object”. In: *Journal of Microscopy* 206.1 (2002), pp. 33–40. ISSN: 1365-2818. DOI: 10.1046/j.1365-2818.2002.01010.x.
- [78] Anna Burvall et al. “Phase Retrieval in X-ray Phase-Contrast Imaging Suitable for Tomography”. In: *Optics Express* 19.11 (May 2011), pp. 10359–10376. ISSN: 1094-4087. DOI: 10.1364/OE.19.010359.
- [79] Lorenz Birnbacher, Manuel Viermetz, and Wolfgang Noichl. *X-Ray Computed Tomography*. Oct. 2019.
- [80] J. Pfaff et al. “In Situ Chamber for Studying Battery Failure Using High-Speed Synchrotron Radiography”. In: *Journal of Synchrotron Radiation* 30.1 (Jan. 2023), pp. 192–199. ISSN: 1600-5775. DOI: 10.1107/S1600577522010244.
- [81] ESRF Data Analysis Unit. *Nabu, ESRF Tomography Processing Software*.
- [82] Mehmet Sezgin and Bülent Sankur. “Survey over Image Thresholding Techniques and Quantitative Performance Evaluation”. In: *Journal of Electronic Imaging* 13.1 (Jan. 2004), pp. 146–165. ISSN: 1017-9909, 1560-229X. DOI: 10.1117/1.1631315.
- [83] Geert Litjens et al. “A Survey on Deep Learning in Medical Image Analysis”. In: *Medical Image Analysis* 42 (Dec. 2017), pp. 60–88. ISSN: 1361-8415. DOI: 10.1016/j.media.2017.07.005.
- [84] Olaf Ronneberger, Philipp Fischer, and Thomas Brox. “U-Net: Convolutional Networks for Biomedical Image Segmentation”. In: *Medical Image Computing and Computer-Assisted Intervention – MICCAI 2015*. Ed. by Nassir Navab et al. Lecture Notes in Computer Science. Cham: Springer International Publishing, 2015, pp. 234–241. ISBN: 978-3-319-24574-4. DOI: 10.1007/978-3-319-24574-4_28.
- [85] Suman Sedai et al. “Semi-Supervised Segmentation of Optic Cup in Retinal Fundus Images Using Variational Autoencoder”. In: *Medical Image Computing and Computer-Assisted Intervention - MICCAI 2017*. Ed. by Maxime Descoteaux et al. Lecture Notes in Computer Science. Cham: Springer International Publishing, 2017, pp. 75–82. ISBN: 978-3-319-66185-8. DOI: 10.1007/978-3-319-66185-8_9.
- [86] Matteo Venturelli. *Fasttomo Repository*. <https://github.com/venturellimatteo/fasttomo>. Feb. 2024.
- [87] Jannis Ahlers et al. *Napari: A Multi-Dimensional Image Viewer for Python*. Zenodo. July 2023. DOI: 10.5281/zenodo.8115575.

- [88] Blender Online Community. *Blender - a 3D Modelling and Rendering Package*. Sept. 2023.
- [89] Morton B. Brown and Alan B. Forsythe. “Robust Tests for the Equality of Variances”. In: *Journal of the American Statistical Association* 69.346 (June 1974), pp. 364–367. ISSN: 0162-1459. DOI: 10.1080/01621459.1974.10482955.
- [90] F. Torabi and V. Esfahanian. “Study of Thermal–Runaway in Batteries I. Theoretical Study and Formulation”. In: *Journal of The Electrochemical Society* 158.8 (May 2011), A850. ISSN: 1945-7111. DOI: 10.1149/1.3592486.
- [91] Qingsong Wang, Ping Ping, and Jinhua Sun. “Catastrophe Analysis of Cylindrical Lithium Ion Battery”. In: *Nonlinear Dynamics* 61.4 (Sept. 2010), pp. 763–772. ISSN: 1573-269X. DOI: 10.1007/s11071-010-9685-7.
- [92] Kazuo Onda et al. “Thermal Behavior of Small Lithium-Ion Battery during Rapid Charge and Discharge Cycles”. In: *Journal of Power Sources* 158.1 (July 2006), pp. 535–542. ISSN: 0378-7753. DOI: 10.1016/j.jpowsour.2005.08.049.
- [93] Hui Yang et al. “Investigations of the Exothermic Reactions of Natural Graphite Anode for Li-Ion Batteries during Thermal Runaway”. In: *Journal of The Electrochemical Society* 152.1 (Nov. 2004), A73. ISSN: 1945-7111. DOI: 10.1149/1.1836126.
- [94] Ping Ping et al. “Thermal Behaviour Analysis of Lithium-Ion Battery at Elevated Temperature Using Deconvolution Method”. In: *Applied Energy* 129 (Sept. 2014), pp. 261–273. ISSN: 0306-2619. DOI: 10.1016/j.apenergy.2014.04.092.

A | LIB energy balance

Semenov model allows a simple and clear interpretation of the thermal runaway process, in which the heat generated by the reactions is the key issue. The heat generation is due to chemical and electrochemical reactions and Joule heating inside the battery. The heat dissipation to the ambient is controlled by radiation and convection. In general, the energy balance between the heat generation and dissipation can be described as follows [34, 90]:

$$\frac{\partial(\rho C_p T)}{\partial t} = -\nabla(k \nabla T) + Q_{\text{ab-chem}} + Q_{\text{joul}} + Q_S + Q_p + Q_{\text{ex}} \quad (\text{A.1})$$

where ρ [g cm^{-3}] is the density, C_p [$\text{J g}^{-1} \text{ K}^{-1}$] is the heat capacity, T [K] is the temperature, t [s] is the time and k [$\text{W cm}^{-1} \text{ K}^{-1}$] is the thermal conductivity. $Q_{\text{ab-chem}}$ is the abuse chemical reaction heat in the battery (reactions will be discussed in detail in Appendix B), Q_{joul} is the Joule heating in the battery, Q_S is the entropy change heat, Q_p is the overpotential heat and Q_{ex} is the heat exchange between the system and the ambient.

The reaction heat generation is the total result of all possible reactions when the battery is undergoing a thermal runaway, mainly including SEI decomposition, electrodes reaction with electrolyte, electrodes decomposition. For the individual reaction, the heat generation can be expressed as $Q_{\text{ab-chem}}$ [91]:

$$Q_{\text{ab-chem}} = \frac{dH}{dt} = \Delta H M^n A \exp\left(-\frac{E_a}{RT}\right) \quad (\text{A.2})$$

where ΔH is the heat of reaction, M is the mass of the reacting material, n is the reaction order, A is the pre-exponential factor, E_a is the activation energy, R is the gas constant and T is the temperature. The total heat generation is the summarized value of all the reactions in the battery.

When a current flows through a device it induces Joule heating. In a lithium-ion battery, the electrical resistance consists of the resistance of the positive and negative electrodes,

electrolyte and separator. In each region, the current passes through different phases, hence Joule heating should be considered in all the phases. Therefore, Joule heating can be written as [90]:

$$Q_{\text{joul}} = \sum_j |\phi_j \cdot i_j| \quad (\text{A.3})$$

where ϕ_j and i_j represent the electric potential [V] and current density [A cm^{-2}] in phase j , respectively. In this equation, the absolute value signs should be present since Joule heating is always positive and contributes to a rise in temperature.

The heat Q_S by entropy change is described by the following equation [92]:

$$Q_S = IT \frac{\partial E_{\text{emf}}}{\partial T} \quad (\text{A.4})$$

where T is the battery temperature, I is the charge/discharge current (defined as positive during charge cycle) and E_{emf} is the cell potential for open-circuit. The reaction directions for charge and discharge cycles are opposite to each other, thus Q_S is endothermic for charge cycle and exothermic during discharge cycle.

When electric current flows through the cell, cell voltage V deviates from open-circuit potential V_0 due to electrochemical polarization. The energy loss by this polarization dissipates as heat. This overpotential heat Q_P is described as following equation [92]:

$$Q_P = I(V - V_0) = I^2 R\eta \quad (\text{A.5})$$

where Q_P is exothermic during both charge and discharge cycles. When the difference between V and V_0 is expressed as $IR\eta$, Q_P can be determined from the overpotential resistance $R\eta$.

The radiation and the convection heat transfer are the main thermal exchanges between the cell surface and environments. When the battery temperature exceeds the ambient temperature, the convection starts to dissipate the thermal energy. When the battery is working at low temperatures, the effect of radiation can be neglected. But in high temperature batteries, radiation plays an important role and should be considered. Convective and radiative heat flux out to ambient are evaluated in the following equations [90]:

$$Q_{\text{conv}} = hA(T_{\text{surf}} - T_{\text{amb}}) \quad (\text{A.6})$$

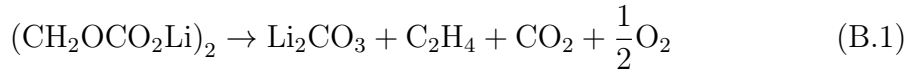
$$Q_{\text{rad}} = \sigma \varepsilon A (T_{\text{surf}}^4 - T_{\text{amb}}^4) \quad (\text{A.7})$$

where h is the convective heat transfer coefficient, A is the surface area of the battery case, T_{surf} is the surface temperature of the battery, T_{amb} is the ambient temperature, σ is the Stefan-Boltzmann constant and ε is the emissivity of the battery surface.

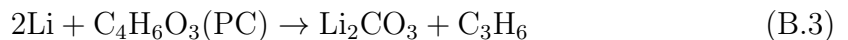
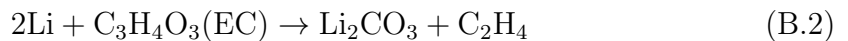
B | LIB chemical reactions

The term $Q_{ab\text{-chem}}$ involves several stages contributing to the buildup of the thermal runaway, and each one causes progressively more permanent damage to the cell. As temperature increases, the battery undergoes the following chemical transformations: SEI layer decomposition, reaction between the anode material and electrolyte, reaction between the cathode material and electrolyte, electrolyte decomposition and reaction between the anode and the binder [34]. Many of them may occur in parallel.

- Breakdown of SEI layer:** The initial phase of a thermal runaway reaction involves the deterioration of the slender SEI layer, with the transformation taking place between 90-120 °C. This process emits CO₂ as per the following reaction [93]:

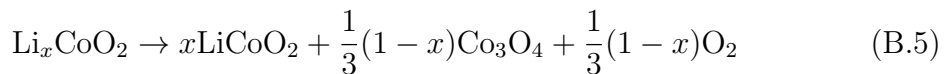


- Reaction between anode and electrolyte:** The breakdown of the SEI layer not only generates heat within the battery but also leads to a reaction between the electrolyte and the carbon anode, as the anode is left unprotected due to the loss of the SEI layer's shielding. These reactions release flammable hydrocarbon gases (ethane, methane and others) but no oxygen.



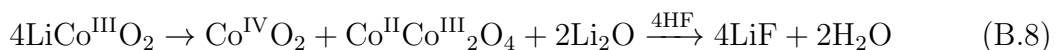
This typically starts at 100 °C but with some electrolytes it can be as low as 68 °C. The gas generation due to the breakdown of the electrolyte causes pressure to build up inside the cell. Although the temperature increases to beyond the flashpoint of the gases released by the electrolyte the gases do not burn because there is no free oxygen in the cell to sustain a fire.

3. **Collapse of the separator and formation of the ISC:** Most separators melt between 130 °C and 200 °C. With rising temperatures, the separator shrinks even more, potentially causing the cathode and anode to come into contact with each other, thereby creating an internal short circuit (ISC). ISC serves as a significant trigger for thermal runaway, and the electrical energy discharged during thermal runaway is roughly equivalent to the energy stored within the battery.
4. **Decomposition of the cathode and reaction with the electrolyte:** As the temperature increases, the cathode starts to break down and emit oxygen. The temperatures at which self-sustaining exothermic reactions begin are 150, 199, and 310 °C for LCO, NCM, and LFP cathodes (each charged to 4.2 V versus Li metal), respectively. The decomposition reactions for the above mentioned cathodes are reported below:



Equation B.6 shows NCM conversion from a layered structure (space group $\text{R}\bar{3}m$) to a MO-type rock salt phase ($\text{Fm}\bar{3}m$) and a metallic phase.

5. **Decomposition of the electrolyte:** The released oxygen reacts with the solvents, both organic and inorganic. When the temperature exceeds 200 °C, the electrolyte will also decompose exothermically and release carbon dioxide, fluoride gases and hydrocarbons. As these reactions take place and gaseous decomposition products accumulate, the pressure inside the LIB rises leading to the activation of a safety valve. The released gases may readily ignite and further increase hazards associated with the thermal runaway.
6. **Reaction related to the binder:** When the battery temperature is above 260 °C, the binder can react with the cathode material and Li_xC_6 . At elevated temperature, the formation of surface Co_3O_4 and dissolution of Co ions is accelerated at the interface between the active material and the binder. Hydrogen fluoride, HF, was found to be involved in the disproportionation reaction of LCO:



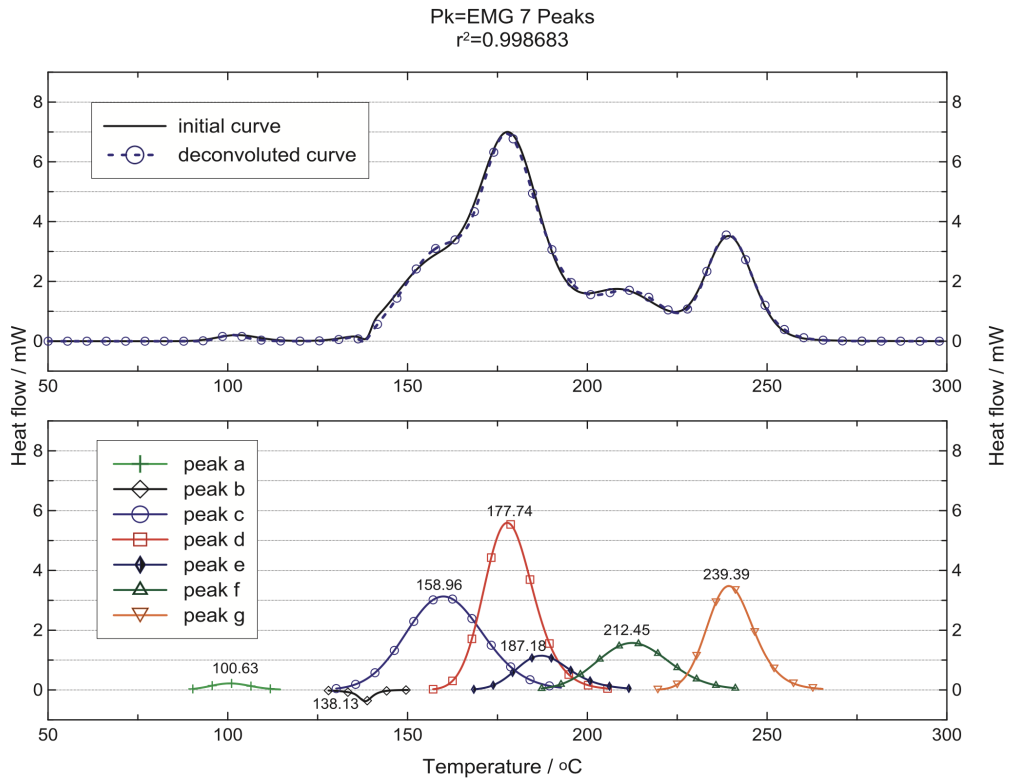


Figure B.1: Initial and deconvoluted heat flow curves of heat flow versus temperature of full cell at $0.2\text{ }^{\circ}\text{C min}^{-1}$. Source: Ping (2014) [94].

Peak	Onset temperature [$^{\circ}\text{C}$]	Corresponding reaction	Heat release [mJ]	Specific Heat release [J g^{-1}]
a	89.06	Decomposition of SEI layer	-1077.66	-44.90*
b	127.79	Separator melting	943.74	224.70***
c	129.35	Cathode-anode materials internal short circuit	-25615.66	-
d	158.08	Li_xCoO_2 disproportionation	-29340.06	-488.18**
e	169.16	Lithium (in Li_xC_6)-electrolyte reaction	-6652.43	-277.18*
f	188.29	Further decomposition of Li_xCoO_2	-12072.59	-200.88**
g	220.65	Oxidation of the thermal decomposition products of electrolyte/thermal reactions involving PVDF	-17251.04	-718.79*/ -287.04**

Table B.1: Reaction properties of every deconvoluted peak in Figure B.1. *, **, *** is the specific heat release divided by the anode mass, cathode mass and separator mass, respectively. Exothermic heat is negative. Source: Ping (2014) [94].

List of Figures

1.1	2021 Global CO ₂ emissions from fuel combustion by sector	3
1.2	Components of a traditional lithium-ion battery during discharging	5
1.3	Mechanistic model of the SEI	11
1.4	Scanning electron microscopic pictures of separators	13
1.5	Inner structure of lithium-ion cells	15
2.1	Schematic of the causes of lithium-ion battery thermal runaway	19
2.2	Temperature dependence of reaction rate and heat loss	20
2.3	Overview of the overcharge side reactions	23
2.4	Illustration of various mechanical abuse mechanisms	25
3.1	European Synchrotron Radiation Facility accelerators	30
3.2	Schematic illustration of ID19 hutches	32
3.3	Computed tomography scan	33
3.4	Absorption contrast imaging schema	35
3.5	Breast tissue contrast comparison	35
3.6	Phase contrast imaging schema	36
3.7	Filtered backprojection	37
3.8	Fourier slice theorem	39
3.9	Radial frequency distribution	40
3.10	Backprojection reconstruction method for parallel beam tomography	41
3.11	High-speed X-ray imaging setup	43
4.1	P28A before and after TR	45
4.2	Segmentation processes for an idealized sample and a gravel filter pack . .	46
4.3	Threshold computation process	49
4.4	P28A slice <code>ct</code> and <code>mask</code>	50
4.5	Agglomerates features plots	54
4.6	Napari viewer	56
4.7	Blender renders	57

5.1	P28A_Heat_Exp4_2 agglomerate density plot	60
5.2	P28A_Heat_Exp4_2 agglomerate renderings	60
5.3	VCT5A_Nail_Exp4 agglomerate density plot	61
5.4	VCT5A_Nail_Exp4 agglomerate renderings	61
5.5	P28B_ISC slices	62
5.6	P28A and VCT5A agglomerate feature comparison	63
5.7	P28A and VCT5A agglomerate size plots	63
5.8	P28A and VCT5A steady state renderings	64
B.1	Heat flow curves	83

List of Tables

1.1	Commercial alternatives for cobalt oxide	6
1.2	Psycho-chemical characteristics of selected battery solvents	9
1.3	Separators essential properties	12
2.1	Lithium-ion battery accidents	17
2.2	Testing standards comparison	22
2.3	EUCAR hazard levels	26
4.1	Agglomerates extracted features	53
5.1	Agglomerate feature comparison	59
B.1	Thermal runaway reaction properties	83

Acknowledgements

